

An efficient, time-evolving, global MHD coronal model based on COCONUT

H. P. Wang^{1,2}, S. Poedts^{1,3}, A. Lani^{1,4}, M. Brchnelova¹, T. Baratashvili¹, L. Linan¹, F. Zhang^{5,6}, D. W. Hou⁷, and Y. H. Zhou¹

¹ Centre for Mathematical Plasma-Astrophysics, Department of Mathematics, KU Leuven, Celestijnenlaan 200B, 3001 Leuven, Belgium

e-mail: Stefaan.Poedts@kuleuven.be

e-mail: andrea.lani@kuleuven.be

² State Key Laboratory of Space Weather, Chinese Academy of Sciences, Beijing 100190

e-mail: haopeng.wang1@kuleuven.be

³ Institute of Physics, University of Maria Curie-Skłodowska, ul. Radziszewskiego 10, 20-031 Lublin, Poland

⁴ Von Karman Institute For Fluid Dynamics, Waterloosesteenweg 72, 1640 Sint-Genesius-Rode, Brussels, Belgium

⁵ Institute of Theoretical Astrophysics, University of Oslo, PO Box 1029 Blindern, 0315 Oslo, Norway

⁶ Rosseland Centre for Solar Physics, University of Oslo, PO Box 1029 Blindern, 0315 Oslo, Norway

⁷ Department of Automation, University of Science and Technology of China, Hefei 230026

September 4, 2024

ABSTRACT

Context. Magnetohydrodynamic (MHD) solar coronal models are critical in the Sun-to-Earth model chain and the most complex and computationally intensive component, particularly the time-evolving coronal models, typically driven by a series of time-evolving photospheric magnetograms. There is an urgent need to develop efficient and reliable time-evolving MHD coronal models to further improve our ability to predict space weather.

Aims. COCONUT is a rapidly developing MHD coronal model. Adopting the efficient implicit algorithm makes it suitable for performing computationally intensive time-evolving coronal simulations. This paper aims to extend COCONUT to an efficient time-evolving MHD coronal model.

Methods. In this MHD model, as usual, an implicit temporal integration algorithm is adopted to avoid the Courant-Friedrichs-Lewy (CFL) stability restriction and increase computational efficiency by large time steps. The Newton iteration method is applied within each time step to enhance the temporal accuracy. The unstructured geodesic mesh is used for flexibility in mesh division and to avoid degeneracy at the poles. Furthermore, an HLL Riemann solver with a self-adjustable dissipation term accommodates both low- and high-speed flows. A series of time-evolving photospheric magnetograms are utilized to drive the evolution of coronal structures from the solar surface to $25 R_{\odot}$ during two Carrington rotations (CRs) around the 2019 eclipse in an inertial coordinate system. It shows that COCONUT can mimic the coronal evolution during a full CR within 9 hours (1080 CPU cores, 1.5M cells). We also compare the simulation results of time-evolving versus quasi-steady-state coronal simulations in the thermodynamic MHD model to validate the time-evolving approach. Additionally, we evaluate the effect of time steps on the simulation results to find an optimal time step that simultaneously maintains high efficiency and necessary numerical stability and accuracy.

Results. Consequently, we developed the first fully implicit time-evolving coronal model, and this highly efficient model is promising for timely and accurately simulating the time-evolving corona in practical space weather forecasting.

Key words. Sun: magnetohydrodynamics (MHD) –methods: numerical –Sun: corona

1. Introduction

Space weather refers to the variable physical conditions on the Sun and in the solar wind, magnetosphere, ionosphere, and thermosphere of the Earth. It can influence the performance and reliability of space-borne and ground-based technological systems and affect human life and health. Since humanity entered the electric age, the economic losses caused by severe space weather have been enormous and continue to increase. There is thus an urgent need to develop advanced Sun-to-Earth model chains to understand the mechanisms of space weather and ultimately provide reliable space weather forecasts hours to days in advance (e.g., Baker 1998; Feng et al. 2011a, 2013a; Feng 2020b; Koskinen et al. 2017; Singer et al. 2001; Siscoe 2000). The physically based MHD modeling is the first prin-

cipal method capable of bridging large heliocentric distances from near the Sun to well beyond Earth’s orbit self-consistently (e.g., Detman et al. 2006; Dryer 2007; Feng et al. 2007, 2014b, 2010, 2011b, 2012a,b, 2014a, 2017; Feng 2020b; Gombosi et al. 2018; Hayashi et al. 2006; Li & Feng 2018; Li et al. 2020; Lugaz & Roussev 2011; Mikić et al. 1999; Nakamizo et al. 2009; Riley et al. 2012; Shen et al. 2021; Tóth et al. 2012; Usmanov 1993; Usmanov & Goldstein 2003; Wu & Dryer 2015; Yang et al. 2021; Zhou et al. 2012; Zhou & Feng 2017). However, realistic MHD simulations of the large solar-terrestrial system are complex, involving various physical phenomena across diverse spatiotemporal scales, and are very computationally intensive. We need to develop more efficient and reliable MHD models to improve our ability to timely and accurately predict

space weather (e.g., Feng 2020b; Owens et al. 2017, and references therein).

Since the solar-terrestrial space is vast and involves diverse spatiotemporal scale phenomena, and it is difficult to use a single model to simulate the significantly different physical phenomena across the entire solar-terrestrial space, coupling different models dedicated to specific regions and physical problems has become the preferred approach for establishing a space weather forecasting framework (e.g., Feng et al. 2013a; Goodrich et al. 2004; Hayashi et al. 2021; Kuřma et al. 2023; Odstrcil et al. 2004; Perri et al. 2022, 2023; Poedts, S. et al. 2020; Tóth et al. 2012). In the coupled Sun-to-Earth model chain, the observed photospheric magnetic fields serves as input data to the solar coronal model, the solar coronal model provides the inner boundary conditions for the inner heliosphere model. The inner heliosphere model gives boundary information to the geomagnetic model. Among these components, the solar coronal model is crucial for determining the initialization of the remaining models, and it is also a key factor affecting the simulation results of solar disturbance propagation and evolution (Brchnelova et al. 2022; Perri et al. 2023). In addition, the solar wind is increased from subsonic/sub-Alfvénic to supersonic/super-Alfvénic in the solar coronal region and the solar disturbances such as coronal mass ejections (CMEs) and solar proton events also propagate through this channel (Feng 2020b; Kuřma et al. 2023).

Though the solar corona is a crucial link in the Sun-to-Earth model chain and significantly impacts the ultimate effects of space weather on our technology, physics-based MHD coronal models are also the most complex and computationally intensive component. For example, a steady-state global solar coronal simulation ranging from 1 to 20 R_s consisting of about 1 M cells and calculated by an explicit MHD model which utilized a solenoidality-preserving approach to maintain magnetic field divergence-free constraints takes about 50 hrs of computing time on 576 MPI processes to obtain a steady-state solution (Feng et al. 2019). Also, a steady-state global solar coronal simulation ranging from 1 to 50 R_s consisting of 4.1 M cells and calculated by an explicit code costs about 100 thousand CPU hours to converge to a quasi-steady state (Réville et al. 2020). In these simulations, the time step is limited to a few seconds due to the restriction of the Courant-Friedrichs-Lewy (CFL) stability condition, which states that the time step length should be limited by the size of the spatial mesh divided by the fastest wave speed (times a constant of order 1). Consequently, researchers have to make many simplifications in solar coronal modeling for the sake of high efficiency. For instance, the empirical based Wang-Sheeley-Argé (WSA) solar coronal model (Argé et al. 2003; Yang et al. 2018) in EUHFORIA (Poedts, S. et al. 2020; Pomoell & Poedts 2018). However, the empirical solar coronal models discard a lot of important information, and it has been demonstrated that even a simple MHD model provides better forecasts (Samara et al. 2021). Therefore, more efforts are required to establish more efficient and accurate MHD solar coronal models.

In recent decades, many researchers have been working on maintaining the positivity-preserving (PP) property of thermal pressure and density in MHD solar coronal simulations. For example, a self-adjusting PP reconstruction method, originally proposed by Balsara (2012) for solving hydrodynamic and magnetohydrodynamic equations, has been implemented in solar coronal simulations by Feng et al. (2017). It was applied to conservative variables via a flattener function defined according to the rarefactive and compressive motions of flow. Furthermore, Feng et al. (2021) and Wang et al. (2022a) extended this

method to primitive variables and implemented it in implicit MHD coronal models. In recent years, some PP Harten-Lax-van Leer (HLL) Riemann solvers (Wu & Shu 2019) are used to design PP MHD coronal models (Feng et al. 2021; Wang et al. 2022a). Although the HLL-family approximate Riemann solvers (e.g., Feng 2020a, and references therein) perform well in preserving PP property for compressible high-speed flow with large Mach number, their diffusion is excessive for the incompressible low-speed flow with a small Mach number. Therefore, a suitable low-dissipation numerical flux solver is desired for low-speed flows to avoid degradation of solution accuracy (e.g., Esquivel et al. 2010; Kitamura et al. 2011; Kitamura & Balsara 2018; Minoshima et al. 2020; Minoshima & Miyoshi 2021; Wang et al. 2022a). It can be seen that the approximate reconstruction method and flux solver are beneficial to maintain PP property of MHD models. In this paper, under the cell-centered finite-volume framework of COCONUT, we implement Venkatakrishnan limiter (Venkatakrishnan 1993) in the reconstruction formula of primitive variables as did before to control spatial oscillation. Furthermore, we design an HLL Riemann solver with a self-adjustable dissipation term to accommodate both low- and high-speed flows.

Additionally, Brchnelova et al. (2023) improved the PP property of COCONUT by manipulating the inner-boundary density according to the local Alfvénic velocity. In this method, the active region density was carefully increased to avoid an abnormally large Alfvénic speed when the local inner-boundary Alfvénic velocity exceeds a prescribed maximum Alfvénic speed. By implementing this method, some non-physical negative thermal pressures and very high-speed streams developed in the domain above the active regions (Kuřma et al. 2023) can be avoided. Consequently, the performance, both in terms of convergence and physical accuracy, can be improved. To enhance the PP property of this time-evolving MHD coronal model, we further extend this method to all the computational domains and apply a smooth hyperbolic tangent function to gradually increase the plasma density when the local Alfvénic speed exceeds 2000 Km/S. In the future, we can take some extra measures, such as the self-adjusting PP reconstruction method (Feng et al. 2021; Wang et al. 2022a) and the incorporation of mass flux limitation (Hayashi 2005; Yang et al. 2012), to further enhance the PP property of COCONUT.

Moreover, reducing the magnetic field discretization error is also helpful in maintaining the PP property of MHD models in low β regions. Considering that $(\mathbf{B} + \epsilon \mathbf{B})^2 - \mathbf{B}^2 \equiv 2 \epsilon \mathbf{B}^2 + \epsilon^2 \mathbf{B}^2$ with $\epsilon \mathbf{B}$ denoting the magnetic field discretization error, the magnetic pressure discretization error can be comparable to thermal pressure in low β (the ratio of the thermal pressure to the magnetic pressure) regions and non-physical negative thermal pressure are prone to appear when deriving thermal pressure from energy density. To avoid such an undesirable situation, some researchers try to decrease the magnetic field discretization error by adopting fine meshes near the solar surface. For Alfvén Wave Solar atmosphere Model (AWSOM), a spherical grid ranging from 1 R_s to 24 R_s is used for the coronal component and the grid is highly refined in the radial direction toward the Sun with the smallest radial grid spacing been approximately 700 Km and the total number of cells been 29.7 M in van der Holst et al. (2022). For the Magnetohydrodynamic Algorithm outside a Sphere (MAS) model, a nonuniform spherical grid consisting of 27.3 M cells and covering a radial range from 1 R_s to 30 R_s is used in Caplan et al. (2017). It is highly non-uniform in the radial direction, and the smallest cell size in the radial direction is 340 Km. In this paper, we adopt the unstruc-

tured geodesic mesh (Brchnelova et al. 2022; Perri et al. 2022) consisting of 1.5 M cells and covering a radial range from 1 R_s to 25 R_s . The grid is gradually stretched in the radial direction with an initial grid spacing of about 170 Km at the solar surface. Besides, an icosahedron-based surface discretization is implemented to cover the sphere with triangular elements with minor variations.

On the other hand, we should strive to improve the computational efficiency of MHD coronal models. As we see, both optimizations for hardware architectures (Caplan et al. 2019; Feng et al. 2013b; Wang et al. 2019b) and efficient algorithms (Feng et al. 2021; Perri et al. 2022, 2023; Wang et al. 2019a, 2022a,b) can significantly improve the computational efficiency of high-performance computational MHD coronal models. Actually, the demand for supercomputing resources continues to grow, often exceeding the capabilities of available hardware architectures. Consequently, further enhancing the computational efficiency of MHD coronal models increasingly relies on developing more efficient algorithms. For instance, by solving the plasma parameters along the fixed potential magnetic field lines from 1 D equations for the plasma motion and heat transport together with the Alfvénic wave propagation in the low coronal region and interfacing this threaded-field-line model with the full MHD global corona model at 1.1 R_s , Sokolov et al. (2021) made the updated AWSoM model, AWSoM-R (AWSoM-realtime), achieve a faster-than-real-time performance on 200 CPU cores. However, the original AWSoM model required 1000-2000 CPU cores to run faster than real-time (Jin et al. 2017). Although effective, this simplification is only applicable to specific issues. More generally, implicit strategies for temporal discretization can be used to loosen the time-step limitation imposed by the CFL stability restriction, thereby enhancing the computational efficiency by utilizing a larger time step.

Recently, several successful attempts have been made to increase the efficiency of MHD coronal models by using implicit solvers. For instance, Wang et al. (2019b) achieved speedup ratios of 31.27 \times and 28.05 \times in MHD solar coronal simulations with an effective matrix-free implicit scheme. It reduces the computational time for the steady-state solar wind study from several days to only a few hours. Feng et al. (2021) and Wang et al. (2022a,b) further improved the implicit method and developed a very efficient parallel lower-upper symmetric Gauss-Seidel (LU-SGS) matrix solver. It reduced the wall-clock times of steady-state MHD coronal simulations from several days to less than 1 hour, even with a plasma β smaller than 10^{-4} . Also, COolfluid COroNal UnSTructured (COCONUT), a novel MHD solar coronal model based on the Computational Object-Oriented Libraries for Fluid Dynamics (COOLFluid)¹, gained a speed up of 35X compared to the state-of-the-art time-explicit Wind-Predict model (Perri et al. 2018) that is based on the PLUTO code (Mignone et al. 2007), while achieving the same level of accuracy in steady-state simulation (Perri et al. 2022, 2023). In addition, the CME simulations (Guo et al. 2023; Linan et al. 2023) demonstrate that the time-dependent COCONUT, which adopts sub-iterations during each physical time step to improve temporal accuracy, has the potential to still be faster than the explicit MHD SC models in time-dependent simulations while maintaining time-accurate using a suitable time step. What's more, Wang et al. (Submitted) proposed a more efficient time-accurate implicit MHD model of the solar corona and CMEs. It was demonstrated to be capable of timely and accurately simulating time-varying events in the solar corona,

even with low plasma beta. Besides, the fully implicit scheme of Block-Adaptive Tree Solarwind Roe-type Upwind Scheme (BATS-R-US) code (Tóth et al. 2012), the explicit scheme of which was used by AWSoM coronal model, can also produce speedup ratios of order 10-20 compared to the explicit version in simulations of some geophysical applications (Tóth et al. 2006, 2008). However, these coronal models are still steady-state models.

After gaining significant improvements in computational efficiency, and with the epoch of fine spatio-temporal resolution observations on the horizon (McCrea & Rae 2019; Srivastava et al. 2021), it's time to extend these efficient steady-state coronal models to more realistic time-evolving versions. Steady-state coronal models assume that the solar coronal structure doesn't change obviously during one Carrington rotation period and use a time-invariant photospheric magnetic field as an inner boundary to generate a steady-state coronal structure. This simplification differs from the reality that the solar coronal structure evolves over time (Owens et al. 2017) and leads to discrepancies between the simulation results and observations of the solar coronal structures (Cash et al. 2015; Réville et al. 2020). Unlike steady-state coronal models, time-evolving coronal models are driven by typically hundreds of time-evolving observed photospheric magnetograms and can achieve time-evolving features of the large-scale coronal structures with higher fidelity (Feng et al. 2023; Yang et al. 2012), and such a technique of time-evolving coronal modeling may be particularly relevant for the next generation of solar wind and CME models (Lionello et al. 2023).

In the last decades, many researchers have worked on developing and improving time-evolving coronal models. For instance, Detman et al. (2006), Linker et al. (2016) and Merkin et al. (2016) used a time series of photospheric magnetograms to drive an empirical source surface current sheet coronal model to provide time-evolving lower boundary conditions for the inner heliosphere MHD solar wind model. These hybrid Sun-to-Earth modeling systems are very efficient for real-time operations but fail to produce coronal transient events or mimic closed loops that rise beyond the source surface (usually between 2.0 and 2.5 R_s). Furthermore, Hoeksema et al. (2020) and Hayashi et al. (2021) employed the electric field derived at the Sun's photosphere from a sequence of vector magnetogram and Doppler velocity measurements (Fisher et al. 2020) to drive a magnetofrictional (MF) model, and then used the MF model to produce time-evolving boundary magnetic fields at 1.15 R_s for their global coronal-heliospheric MHD (GHM) model. Although the MF model can be very numerically stable in generating time-dependent three-dimensional coronal magnetic structures, it failed to provide the required initial dynamic states of the plasma in the low atmosphere. To ensure the boundary plasma quantities at 1.15 R_s evolve consistently with both the variations of the magnetic field specified from the MF model and the governing MHD equations of the GHM model, they employed the projected normal characteristics method (e.g. Sauerwein 1966) at the interface boundary. Besides, Feng et al. (2023) and Yang et al. (2012) specified the tangential boundary electric field to make the flux evolution match the changes of the observed radial magnetic field and employed the projected normal characteristic method to make boundary conditions self-consistent. In addition, Feng et al. (2012a), Lionello et al. (2023) and Mason et al. (2023) employed the surface flux transport model (DeVore et al. 1984; Schrijver & DeRosa 2003) to obtain input maps that incorporate magnetic flux emergence and surface flows for their MHD coronal models.

¹ <https://github.com/andrealani/COOLFluid.git>

Among these time-evolving coronal models mentioned above, MAS (Lionello et al. 2023; Mason et al. 2023) adopts a semi-implicit approach where only some source terms are treated implicitly, and the time step needs to be chosen in accordance with the limitations imposed by the explicitly treated terms (Feng 2020a). Feng et al. (2023) used the fully implicit method (Feng et al. 2021; Wang et al. 2022a) only at the 6-layer grid close to the solar surface in the radial direction and reported that it helped to avoid the occurrence of negative density and pressure caused by the strong magnetic field near the Sun. The remaining models still use explicit methods. Obviously, the current time-evolving coronal models can be much more efficient and numerically stable for practical application works by appropriately adopting fully implicit algorithms.

In this paper, based on the time-dependent COCONUT coronal model, we further design an HLL Riemann solver with a self-adjustable dissipation term to accommodate both low- and high-speed flows, take some PP measures to make the model more numerically stable, and use cubic Hermite interpolation to derive the time-evolving magnetograms at each physical time step. Finally, we develop an efficient time-evolving MHD coronal model driven by a series of time-evolving magnetograms and the model has flexibility in selecting large time steps. This model is expected to be used to provide inner-boundary conditions for the inner heliosphere models in practical space weather forecasting. As we know, most MHD inner heliosphere models adopt explicit numerical schemes, and their time steps, limited by the CFL stability criterion, are typically on the order of 10 minutes (Detman et al. 2006; Hayashi 2012). This time-step size is much larger than that in explicit MHD coronal models. It requires the coronal models to perform significantly more calculations to maintain synchronization with the inner heliosphere models. Consequently, MHD coronal models become the most computationally intensive component in the Sun-to-Earth model chain. Therefore, we try to enhance flexibility in selecting the time step for our time-evolving MHD coronal model. It will allow us to adjust the time steps in coronal simulations to match those used in the inner-heliosphere models. In this way, the MHD coronal model, with time steps determined by the inner heliosphere model, will be able to provide the required accurate inner-boundary conditions for the inner heliosphere model while maintaining high efficiency. This approach will also make it easier to mimic the entire solar-terrestrial domain with a single tool, which can simplify the Sun-to-Earth modeling process.

Based on the above considerations, the paper is organized as follows. In Section 2, we introduce the governing equations, grid system, and initial conditions adopted in the solar coronal simulations. In Section 3, the numerical formulation of the time-evolving coronal simulations is described in detail. This section mainly describes the discretization of the MHD equations, the implementation of time-evolving boundary conditions, the HLL Riemann solver with a self-adjustable dissipation term, and the PP measures used to enhance the coronal model's numerical stability. In Section 4, we demonstrate the simulation results. In this section, the evolution of the corona during two CR periods around the 2019 eclipse mimicked by the time-evolving COCONUT is demonstrated, a comparison of the 2019 eclipse simulations performed by both the time-evolving COCONUT and its quasi-steady-state version is illustrated, the simulation results calculated with different time-step sizes are also compared. In Section 5, we summarize the main features of the efficient, fully implicit, time-evolving coronal model and give some concluding remarks.

2. Governing equations and grid system

This section mainly describes the governing equations, grid system, and initial conditions used for the simulation of quasi-steady-state coronal and time-evolving coronal simulations.

2.1. The governing equations

In this paper, based on the time-dependent COCONUT coronal model (Perri et al. 2022; Baratashvili et al. Submitted), we further develop the time-evolving version of COCONUT to make time-evolving coronal simulations. First, we initiate a quasi-steady-state coronal simulation constrained by a fixed magnetogram to get the background corona. Once the steady-state simulation converges, we drive the subsequent evolution of the dynamic corona by a series of time-evolving photospheric magnetograms. The governing MHD equations are calculated in the Heliocentric Inertial (HCI) coordinate system (Burlaga 1984; Fränz & Harper 2002), and reads as follows.

$$\frac{\partial \mathbf{U}}{\partial t} + \nabla \cdot \mathbf{F}(\mathbf{U}) = \mathbf{S}(\mathbf{U}, \nabla \mathbf{U}). \quad (1)$$

Here $\mathbf{U} = (\rho, \rho \mathbf{v}, \mathbf{B}, E, \psi)^T$ denotes the conservative variable vector, $\nabla \mathbf{U}$ corresponds to the spatial derivative of \mathbf{U} , the inviscid flux vector $\mathbf{F}(\mathbf{U})$ is defined as below

$$\mathbf{F}(\mathbf{U}) = \begin{pmatrix} \rho \mathbf{v} \\ \rho \mathbf{v} \mathbf{v} + \left(p + \frac{\mathbf{B}^2}{2}\right) \mathbf{I} \\ (E + p_T) \mathbf{v} - \mathbf{B}(\mathbf{v} \cdot \mathbf{B}) \\ \mathbf{v} \mathbf{B} - \mathbf{B} \mathbf{v} + \psi \mathbf{I} \\ V_{\text{ref}}^2 \mathbf{B} \end{pmatrix},$$

and $\mathbf{S}(\mathbf{U}, \nabla \mathbf{U}) = \mathbf{S}_{\text{gra}} + \mathbf{S}_{\text{heat}}$ represents the source term vector corresponding to the gravitational force and the heating source terms defined as below

$$\mathbf{S}_{\text{gra}} = -\frac{\rho G M_s}{|\mathbf{r}|^3} \begin{pmatrix} 0 \\ \mathbf{r} \\ \mathbf{0} \\ \mathbf{r} \cdot \mathbf{v} \\ 0 \end{pmatrix}, \quad \mathbf{S}_{\text{heat}} = \begin{pmatrix} 0 \\ \mathbf{0} \\ \mathbf{0} \\ -\nabla \cdot \mathbf{q} + Q_{\text{rad}} + Q_H \\ 0 \end{pmatrix}. \quad (2)$$

In these formulations mentioned above, $\mathbf{B} = (B_x, B_y, B_z)$ and $\mathbf{v} = (u, v, w)$ denote the magnetic field and velocity in Cartesian coordinate system, $E = \frac{p}{\gamma-1} + \frac{1}{2}\rho v^2 + \frac{1}{2}\mathbf{B}^2$ means the total energy density with the adiabatic index $\gamma = \frac{5}{3}$, $p_T = p + \frac{\mathbf{B}^2}{2}$ is the total pressure, ρ and p represent the density and thermal pressure of the plasma, \mathbf{r} is the position vector, $r = |\mathbf{r}|$ denotes the heliocentric distance, and t represents the time. For convenience of description, in the definition of the magnetic field, a factor of $\frac{1}{\sqrt{\mu_0}}$ is absorbed with $\mu_0 = 4 \times 10^{-7} \pi \text{ H m}^{-1}$ denoting the magnetic permeability. As usual, G means the universal gravitational constant, M_s means the mass of the Sun, and $G M_s = 1.327474512 \times 10^{20} \text{ m}^3 \text{ s}^{-2}$. The thermal pressure of the plasma is defined as $p = \mathfrak{R} \rho T$, where T is the temperature of the bulk plasma, $\mathfrak{R} = 1.299 \times 10^4 \text{ m}^2 \text{ s}^{-2} \text{ K}^{-1}$ denotes the gas constant and is calculate by $\mathfrak{R} = \frac{2 * k_B}{m_{\text{cor}} * m_H}$ with $k_B = 1.3806503 \times 10^{-23} \text{ J K}^{-1}$ denoting the Boltzmann constant, the molecular weight set to $m_{\text{cor}} = 1.27$ (Aschwanden 2005) and $m_H = 1.67262158 \times 10^{-27} \text{ Kg}$ representing the mass of hydrogen. We adopt the hyperbolic generalized Lagrange multiplier (GLM) method (Dedner et al. 2002) to constrain the divergence error, ψ and V_{ref} denote the Lagrange multiplier and the propagation speed of the numerical divergence error. In the energy

source term, Q_H , Q_{rad} and $-\nabla \cdot \mathbf{q}$ are used to mimic the coronal heating, radiation loss, and thermal conduction, respectively.

As did in Baratashvili et al. (Submitted), the heat flux \mathbf{q} included in \mathbf{S}_{heat} is defined in a Spitzer form or collisionless form according to the radial distance as below (Hollweg 1978; Mikić et al. 1999)

$$\mathbf{q} = \begin{cases} -\xi T^{5/2} (\hat{\mathbf{b}} \cdot \nabla T) \hat{\mathbf{b}}, & \text{if } 1 \leq r \leq 10R_s \\ \alpha n_e k_B T \mathbf{v}, & \text{if } r > 10R_s \end{cases} \quad (3)$$

Here $\hat{\mathbf{b}} = \frac{\mathbf{B}}{|\mathbf{B}|}$, $\xi = 9.0 \times 10^{-12} \text{Jm}^{-1} \text{s}^{-1} \text{K}^{-7/2}$, α is set to $\frac{3}{2}$ (Lionello et al. 2008) and n_e is the electron number density. The radiative approximation is determined by assuming the radiative losses to be optically thin (Rosner et al. 1978; Zhou et al. 2021),

$$Q_{rad} = -n_e n_p \Lambda(T). \quad (4)$$

where n_e and n_p denote the electron and proton number densities, respectively, and are assumed to be equal for the hydrogen plasma. $\Lambda(T)$ is a temperature-dependent radiative cooling curve function. Similar to van der Holst et al. (2014), $\Lambda(T)$ in this paper is derived from version 9 of CHIANTI (Dere et al. 2019), an atomic database for emission lines, and the profile of $\log(\Lambda(T))$ independent of $\log(T)$, with $\Lambda(T)$ and T in units of $\text{erg s}^{-1} \text{cm}^3$ and K, is demonstrated in Fig. 1. As did in Xia et al.

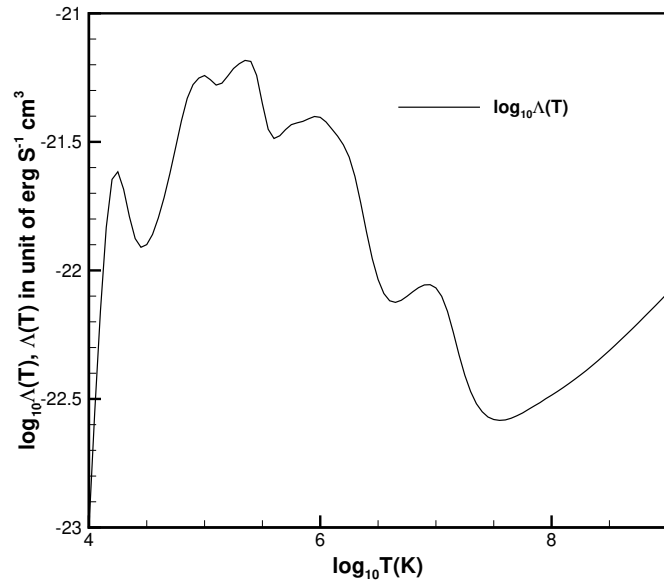


Fig. 1. Radiative cooling curve profile derived from version 9 of CHIANTI (Dere et al. 2019) atomic database. The horizontal axis denotes the decadic logarithm of temperature, and the vertical axis shows the logarithm of the radiative cooling curve function value. The units of temperature and radiative cooling curve function are K and $\text{erg s}^{-1} \text{cm}^3$, respectively.

(2011), we set $\Lambda(T)$ to zero when $T < 2 \times 10^4$ K, which means the plasma has become optically thick and is no longer fully ionized. Although the form of the coronal heating term Q_H strongly affects the plasma density and temperature of the solutions (Lionello et al. 2008), the heating mechanism of the corona is still unclear. Compromisingly, we adopt the following empirical heating source term, which was discussed and recommended in Baratashvili et al. (Submitted). It is proportional to the local

magnetic field strength (Mok et al. 2005) while also exhibiting an exponential decay in the radial direction (Downs et al. 2010).

$$Q_H = H_0 \cdot |\mathbf{B}| \cdot e^{-\frac{r-R_s}{\lambda}}. \quad (5)$$

where $H_0 = 4 \times 10^{-2} \text{J m}^{-3} \text{s}^{-1} \text{Tesla}^{-1}$ and $\lambda = 0.7R_s$.

To make the governing equations more convenient to discretize, the variables \mathbf{r} , ρ , \mathbf{v} , p , \mathbf{B} and t are normalized by R_s , ρ_s , $V_{a,s}$, $\rho_s V_{a,s}^2$, B_s and $\frac{R_s}{V_{a,s}}$, respectively. Here $R_s = 6.95 \times 10^8$ m is the solar radius, $\rho_s = 1.67 \times 10^{-13} \text{Kg m}^{-3}$, $B_s = 2.2 \times 10^{-4}$ Tesla and $V_{a,s} = \frac{B_s}{\rho_s^{1/2}}$ denotes the characteristic plasma density, magnetic field strength and Alfvénic velocity at solar surface, respectively.

2.2. Computational grid system and initializations

The governing equation is numerically solved based on the cell-centered finite-volume method. The computational domain is a spherical shell ranging from 1.01 to $25 R_s$, and we adopt the unstructured 6_{th} -level subdivided geodesic mesh to avoid degeneracy in the polar regions. In this paper, an icosahedron-based surface discretization is implemented to create a geodesic polyhedron with triangular elements. The 3D spherical shell grid is then constructed by stacking the discretized surface radially outward with pre-determined radial intervals. A more detailed description of the grid is available in Brchnelova et al. (2022). In this paper, the computational domain is divided into 1495040 non-overlapped triangular pyramid cells, with each cell consisting of 2 triangular faces and 3 quadrilateral faces, and these cells are distributed to different processors by ParMETIS software package (Karypis 2011). There are 73 layers of gradually stretched cells in the radial direction, and each layer contains 20480 cells with minor variations. It means each inner-boundary face, a patch of the solar surface, can cover a supergranulation or a sunspot.

The observed line-of-sight photospheric magnetic field is assigned to the inner-boundary faces to provide inner-boundary conditions of the magnetic field. The original photospheric magnetic field strength can be hundreds of Gauss near active regions and may cause non-physical negative temperatures or pressures (Kuźma et al. 2023). To avoid such undesired situations, we use a potential-field (PF) solver with spherical harmonic expansions higher than 20 orders neglected to filter the very small-scale structures in the original photospheric magnetograms. Generally, magnetic maps reconstructed by a PF solver of 20-order spherical harmonic expansion are already fully sufficient for the purposes of space weather forecasting (Kuźma et al. 2023). Therefore, we utilize these preprocessed photospheric magnetograms to constrain the coronal simulations in COCONUT (Kuźma et al. 2023; Perri et al. 2022, 2023).

In this paper, we adopt the GONG-zqs photospheric magnetogram, Zero-point Corrected QuickReduce Synoptic Map Data provided by Global Oscillation Network Group observatories (Li et al. 2021; Perri et al. 2023), to constrain the quasi-steady-state coronal simulations and to drive the following time-evolving coronal simulations. At the beginning of the quasi-steady-state coronal simulations, a PF solver with the observed GONG-zqs photospheric magnetogram served as the inner boundary is used to generate the initial magnetic field at all the cell-center points of our mesh. The plasma density ρ , radial speed v_r and thermal pressure p are given by solving Parker's one-dimensional hydrodynamic isothermal solar wind solution (Parker 1963) and the initial temperature and plasma density at

the solar surface are set to be 1.5×10^6 K and 1.67×10^{-13} Kg m⁻³, respectively. After the quasi-steady coronal simulations converge, the time-varying magnetograms are used to drive the following time-evolving coronal simulations. In both quasi-steady-state and time-evolving coronal simulations, the radial magnetic field at the inner-boundary face-center points is linearly interpolated from the magnetogram data. In contrast, the magnetic field within the inner domain determines the tangential component of the magnetic field.

3. Numerical method formulation

In this section, we present the numerical method formulations used in this COCONUT coronal model to reproduce the quasi-steady-state corona and to mimic the following evolution process of the dynamic corona. We briefly describe the discretization of the MHD equations and demonstrate how the inner-boundary conditions are implemented.

In such formulation, a least-square (LSQ) method coupled with a continuously differentiable Venkatakrishnan limiter (Venkatakrishnan 1993) is utilized to reconstruct the piece-wise formula of primitive variables in each cells, a hyperbolic GLM method is adopt to maintain divergence-free constraint of magnetic field, an HLL Riemann solver with a self-adjustable dissipation term is used to calculate numerical flux, the density is appropriately adjusted to avoid the abnormally large Alfvénic speed and thereby enhance the PP property of COCONUT, a fully implicit algorithm is adopted to increase the computational efficiency by enlarging time-step length, the Newton iteration method is applied within each time step of the implicit algorithm to solve the nonlinear equations and improve the temporal accuracy of the implicit solver with time-step length exceeding the CFL condition, and thousands of observed GONG-zqs magnetograms are used to drive the evolution of the dynamic corona in an inertial coordinate system.

As usual, Godunov’s method is used in COCONUT to advance cell-averaged solutions in time by solving a Riemann problem at each cell interface (Einfeldt et al. 1991; Godunov 1959). By integrating Eq. (1) over the pentahedron cell i and using Gauss’s theorem to calculate the volume integral of the divergence of flux, we reach the following discretized equation

$$V_i \frac{\partial \mathbf{U}_i}{\partial t} = - \oint_{\partial V_i} \mathbf{F} \cdot \mathbf{n} d\Gamma + V_i \mathbf{S}_i, \quad (6)$$

where $\oint_{\partial V_i} \mathbf{F} \cdot \mathbf{n} d\Gamma = \sum_{j=1}^5 \mathbf{F}_{ij} \cdot \mathbf{n}_{ij} \Gamma_{ij}$ and $\mathbf{S}_i = \mathbf{S}_{\text{gra},i} + \mathbf{S}_{\text{heat},i}$. Here and hereafter \mathbf{U}_i and \mathbf{S}_i means the cell-averaged solution variable and source term in cell $_i$, V_i is the volume of cell $_i$, Γ_{ij} means the interface shared by cell $_i$ and its neighboring cell cell $_j$, and also denote the area of this interface, $\mathbf{n}_{ij} = (n_{x,ij}, n_{y,ij}, n_{z,ij})$ is the unit normal vector of Γ_{ij} and points from cell $_i$ to cell $_j$. Below we list the formula of $\mathbf{F}_{ij} \cdot \mathbf{n}_{ij}$ with the subscript “ ij ” denoting the corresponding variables on Γ_{ij} . For convenience of description, we describe $\mathbf{F}_{ij} \cdot \mathbf{n}_{ij}$ as $\mathbf{F}_{n,ij}$ here and hereafter.

3.1. Spatial discretization and temporal integration

As usual, approximate Riemann solvers, such as HLL (Feng et al. 2021) and AUSM type (Kitamura 2020; Wang et al. 2022a) solvers, can be used to compute the inviscid flux $\mathbf{F}_{n,ij}$. In this paper, we adopt the HLL Riemann solver. The HLL Rie-

mann solver can be described as below

$$\mathbf{F}_{n,ij}(\mathbf{U}_L, \mathbf{U}_R) = \frac{\mathbf{F}_n(\mathbf{U}_L) + \mathbf{F}_n(\mathbf{U}_R)}{2} - \frac{1}{2} \mathbf{D}_{\text{HLL}}(\mathbf{U}_L, \mathbf{U}_R) \quad (7)$$

with

$$\mathbf{D}_{\text{HLL}}(\mathbf{U}_L, \mathbf{U}_R) = \frac{(S_L + S_R)(\mathbf{F}_n(\mathbf{U}_R) - \mathbf{F}_n(\mathbf{U}_L))}{S_R - S_L} - \frac{2S_R S_L}{S_R - S_L} (\mathbf{U}_R - \mathbf{U}_L) \quad (8)$$

and

$$\mathbf{F}_n(\mathbf{U}) = \begin{pmatrix} V_n \rho \\ V_n \rho u \\ V_n \rho v \\ V_n \rho w \\ (vB_x - B_y u) \cdot n_{y,ij} + (wB_x - B_z u) \cdot n_{z,ij} + \psi_{ij} \cdot n_{x,ij} \\ (uB_y - B_x v) \cdot n_{x,ij} + (wB_y - B_z v) \cdot n_{z,ij} + \psi_{ij} \cdot n_{y,ij} \\ (uB_z - B_x w) \cdot n_{x,ij} + (vB_z - B_y w) \cdot n_{y,ij} + \psi_{ij} \cdot n_{z,ij} \\ V_n (E + p_T) - B_n \mathbf{B} \cdot \mathbf{v} \\ B_n V_{\text{ref}}^2 \end{pmatrix}.$$

Here $V_n(\mathbf{U}) = \mathbf{v} \cdot \mathbf{n}_{ij}$ and $B_n(\mathbf{B}) = \mathbf{B} \cdot \mathbf{n}_{ij}$ denote the velocity and magnetic field along the normal direction of Γ_{ij} , S_L and S_R usually stand for the conventional two fast waves in the HLL Riemann solver (Einfeldt et al. 1991; Gurski 2004). Unless otherwise stated, the subscript “ L ” or “ R ” denote the corresponding left or right variables evaluated on the centroid of Γ_{ij} . In this paper, we set $S_L = \min(0, \lambda_{\min}(\mathbf{U}_L), \lambda_{\min}(\mathbf{U}_R))$ and $S_R = \max(0, \lambda_{\max}(\mathbf{U}_L), \lambda_{\max}(\mathbf{U}_R))$ with

$$\lambda_{\min}(\mathbf{U}) = \min(V_n(\mathbf{U}), V_n(\mathbf{U}) \pm c_{f \text{ or } s}(\mathbf{U}), V_n(\mathbf{U}) \pm c_A(\mathbf{U}))$$

and

$$\lambda_{\max}(\mathbf{U}) = \max(V_n(\mathbf{U}), V_n(\mathbf{U}) \pm c_{f \text{ or } s}(\mathbf{U}), V_n(\mathbf{U}) \pm c_A(\mathbf{U}))$$

where $c_{f \text{ or } s}(\mathbf{U}) = \sqrt{0.5 \left(\frac{\gamma p}{\rho} + \frac{B^2}{\rho} \pm \sqrt{\left(\frac{\gamma p}{\rho} + \frac{B^2}{\rho} \right)^2 - 4 \frac{\gamma p}{\rho} \frac{B_x^2}{\rho}} \right)}$ and

$$c_A(\mathbf{U}) = \frac{|B_n|}{\rho^{0.5}}.$$

Although the HLL Riemann solver performs well in preserving the PP property for compressible high-speed flows with large Mach numbers, its diffusion is excessive for incompressible low-speed flows with small Mach numbers. Therefore, we introduce a factor $\varphi = \frac{\max(S_L, |S_R|)}{S_R - S_L}$ to the second term in RHS of Eq. (8), which plays a major role in low Mach number regions and decreases to zero in high Mach number regions, to reduce the diffusion of HLL Riemann solver for low-speed flow. Consequently, we get the following HLL Riemann solver with a self-adjustable dissipation term,

$$\mathbf{F}_{n,ij}(\mathbf{U}_L, \mathbf{U}_R) = \frac{\mathbf{F}_n(\mathbf{U}_L) + \mathbf{F}_n(\mathbf{U}_R)}{2} - \frac{1}{2} \mathbf{D}'_{\text{HLL}}(\mathbf{U}_L, \mathbf{U}_R) \quad (9)$$

where

$$\mathbf{D}'_{\text{HLL}}(\mathbf{U}_L, \mathbf{U}_R) = \frac{(S_L + S_R)(\mathbf{F}_n(\mathbf{U}_R) - \mathbf{F}_n(\mathbf{U}_L))}{S_R - S_L} - \varphi \frac{2S_R S_L}{S_R - S_L} (\mathbf{U}_R - \mathbf{U}_L) \quad (10)$$

The factor φ will reduce the dissipation term of the HLL Riemann solver by half for low-speed flows and recover to the original one for high-speed flows. We find that introducing this factor improves the numerical stability of our coronal model in our simulations.

As for the cell-averaged source terms in cell_{*i*}, $\mathbf{S}_{\text{gra},i}$ and $Q_{\text{rad},i}$ and $Q_{H,i}$ are calculated by substituting the corresponding variables at the centroid of cell_{*i*} into formulations of \mathbf{S}_{gra} and Q_{rad} and Q_H . Whereas $(\nabla \cdot \mathbf{q})_i$ is calculated by Green-Gauss theorem, $(\nabla \cdot \mathbf{q})_i = \frac{1}{V_i} \sum_{j=1}^5 \mathbf{q}_{ij} \cdot \mathbf{n}_{ij} \Gamma_{ij}$ where $\mathbf{q}_{ij} = \mathbf{q}(T_{ij}, (\nabla T)_{ij}, \mathbf{U}_{ij})$ is the heat flux through Γ_{ij} . In this paper, T_{ij} is derived from the equation of state $T_{ij} = \frac{p_{ij}}{\mathfrak{R}\rho_{ij}}$.

As we see, the plasma states on the cell surface Γ_{ij} are still required in the calculation of the inviscid flux $\mathbf{F}_{n,ij}$ and heat flux $\mathbf{q}_{ij} \cdot \mathbf{n}_{ij}$. For convenience of calculation, we utilize a second-order reconstruction method to calculate the piecewise polynomial of the primitive variable.

$$X_i(\mathbf{x}) = X|_i + \phi_i (\nabla X)|_i \cdot (\mathbf{x} - \mathbf{x}_i) \quad (11)$$

where $X \in \{\rho, u, v, w, B_x, B_y, B_z, p, \psi\}$, $X|_i$ is the corresponding variable at \mathbf{x}_i , the centroid of cell_{*i*}, and $(\nabla X)|_i = \left(\frac{\partial X}{\partial x}, \frac{\partial X}{\partial y}, \frac{\partial X}{\partial z} \right)|_i$ is the derivative of X at \mathbf{x}_i which is calculated by least square method (Barth 1993; Lani 2008), and ϕ_i is the Venkatakrisnan limiter (Venkatakrisnan 1993) used to control spatial oscillation.

In the quasi-steady coronal simulations, we perform a backward Euler temporal integration on Eq. (1) and reach the following equation,

$$V_i \frac{\Delta \mathbf{U}_i^n}{\Delta t} + \mathbf{R}_i(\mathbf{U}^{n+1}) = \mathbf{0}. \quad (12)$$

The superscripts “*n*” and “*n+1*” denote the time level, $\mathbf{R}_i(\mathbf{U}^{n+1}) = \sum_{j=1}^5 \mathbf{F}_{n,ij}(\mathbf{U}_L^{n+1}, \mathbf{U}_R^{n+1}) \Gamma_{ij} - V_i \mathbf{S}_i^{n+1}$ means the residual operator over cell_{*i*} at the (*n* + 1)-th time levels, $\Delta \mathbf{U}_i^n = \mathbf{U}_i^{n+1} - \mathbf{U}_i^n$ is the solution increment between the *n*-th and (*n* + 1)-th time level, and $\Delta t = t^{n+1} - t^n$ is a user-defined time increment. In the quasi-steady coronal simulations, the time variable *t* doesn’t refer to a physical time, but a relaxation time used to implement the time-relaxation iteration to get a quasi-steady state coronal structure.

After reaching a steady-state coronal structure, we utilize a series of time-varying magnetograms to drive the following evolution of the dynamic corona. In time-evolving coronal simulations, in addition to spatial accuracy, we should also consider temporal accuracy. To improve the temporal accuracy of the implicit solver with time-step length exceeding the CFL condition, we adopt the Backward Differentiation Formula of Order 2 (BDF2) for the temporal integration and implement the Newton iteration method within each time step of the implicit algorithm to further enhance the temporal accuracy (Linan et al. 2023). Newton iteration is used to update the intermediate state at each physical time step until the L_2 norm of the differences in state variables between two consecutive iterations decreases to 10^{-3} or after 10 Newton iterations.

Furthermore, to enhance the PP property of COCONUT, the density updated during the Newton iterations is appropriately adjusted according to the local Alfvénic velocity. This manipulation ensures the local Alfvénic velocities calculated from the updated intermediate coronal state are within a reasonable range, thereby improving the PP property of COCONUT. In this adjustment, we apply a smooth hyperbolic tangent function to gradually increase the plasma density when the local Alfvénic speed reaches a prescribed maximum Alfvénic speed, $V_{A,max}$, as follows.

$$\rho = \Upsilon_\rho \frac{\mathbf{B}^2}{V_{A,max}^2} + (1 - \Upsilon_\rho) \rho_o \quad (13)$$

where $\Upsilon_\rho = 0.5 + 0.5 \cdot \tanh\left(\frac{V_A - V_{A,max}}{V_{fac}} \cdot \pi\right)$ with $V_A = \frac{\mathbf{B}}{\rho_o^{0.5}}$, $V_{A,max} = 2000 \text{ Km S}^{-1}$ and $V_{fac} = 2 \text{ Km S}^{-1}$. Here the subscript “*o*” on ρ refers to the density updated in the Newton iteration without adjustment.

3.2. Implementation of boundary conditions

In COCONUT, we adopt one layer of ghost cells near the boundaries (Lani 2008). Near the inner boundary, the variables in ghost cells are defined as below.

$$X_G = 2X_{BC} - X_{inner}, \quad X \in \{\rho, u, v, w, B_x, B_y, B_z, p, \psi\}. \quad (14)$$

where the subscripts “*G*” and *inner* denote the corresponding value in the ghost cell and at the centroid of the nearest cell in the inner domain. In this paper, we set $\psi_{BC} = 0$ (Perri et al. 2022). ρ_{BC} and p_{BC} are defined similar to Brchneleva et al. (2023) to improve PP property of COCONUT.

$$p_{BC} = \Upsilon_p \frac{\mathbf{B}_{BC}^2}{2} \beta_{\min} + (1 - \Upsilon_p) p_s \quad (15)$$

where $\Upsilon_p = 0.5 + 0.5 \cdot \tanh\left(\frac{\beta_{\min} - \frac{p_s}{0.5 \cdot \mathbf{B}_{BC}^2}}{\beta_{fac}} \cdot \pi\right)$ with $\beta_{fac} = 2 \times 10^{-6}$ and $\beta_{\min} = 0.02$. ρ_{BC} is defined as did in Eq. (13), with ρ_o and \mathbf{B} replaced by ρ_s and \mathbf{B}_{BC} . Besides, the inner boundary velocity $\mathbf{v} = (u_{BC}, v_{BC}, w_{BC})$ is defined mainly according to the velocity in the inner domain. The inner-boundary magnetic field is determined by both the observed radial field and the tangential components in the inner domain.

In quasi-steady-state coronal simulations, the radial component of the inner-boundary magnetic field, $B_{BC,r}$, is linearly interpolated from a single magnetogram. For time-evolving coronal simulations, we utilize cubic Hermite interpolation, in which four magnetograms are used as the stencil, to derive an intermediate magnetogram at the corresponding time. The $B_{BC,r}$ is then linearly interpolated from this intermediate magnetogram. Meanwhile, the tangential components $B_{BC,\theta}$ and $B_{BC,\phi}$ are defined as the corresponding values at the centroid of the nearest cell in the inner domain. In this paper, the GONG-zqs synoptic maps are used to drive the evolution of coronal structures in the HCI coordinate system.

The GONG-zqs data is formulated in an inertial coordinate system, and the time interval between two adjacent magnetograms around the 2019 eclipse is around 1 hour with a fluctuation of several minutes. Since it’s more convenient to deal with a batch of the input magnetogram-data files with a constant interval than those with nonuniform intervals, we first perform cubic Hermite interpolations on these observed magnetograms to get a series of magnetograms with a constant interval of 1 hour and then utilize these magnetograms to drive the time-evolving coronal simulations. During the time-evolving coronal simulations, the time-step sizes are set to be several minutes. They are smaller than the time interval between two adjacent magnetograms, thus we perform a cubic Hermite interpolation on these input magnetograms as below to get the required inner-boundary magnetic

field at each time step.

$$\begin{aligned}
B_{BC,r}(t, \theta, \phi) &= h_{00}(t') B_r(\theta, \phi)_m \\
&+ h_{10}(t') (t_{m+1} - t_m) \left(\frac{\partial B_r(\theta, \phi)}{\partial t} \right)_m \\
&+ h_{01}(t') B_r(\theta, \phi)_{m+1} \\
&+ h_{11}(t') (t_{m+1} - t_m) \left(\frac{\partial B_r(\theta, \phi)}{\partial t} \right)_{m+1}
\end{aligned} \tag{16}$$

$$\text{with } t' = \frac{t - t_m}{t_{m+1} - t_m}.$$

Here $B_{BC,r}(t, \theta, \phi)$ is the interpolated magnetic field at the inner-boundary facial centroid located at (R_s, θ, ϕ) , t denotes the physical time, and the subscripts “ m ” and “ $m+1$ ” refer to the m -th and $(m+1)$ -th magnetograms, two adjacent magnetograms nearby t , with $t_m < t \leq t_{m+1}$, $\left(\frac{\partial B_r(\theta, \phi)}{\partial t} \right)_m = \frac{1}{2} \left(\frac{B_r(\theta, \phi)_{m+1} - B_r(\theta, \phi)_m}{t_{m+1} - t_m} + \frac{B_r(\theta, \phi)_m - B_r(\theta, \phi)_{m-1}}{t_m - t_{m-1}} \right)$ and $\left(\frac{\partial B_r(\theta, \phi)}{\partial t} \right)_{m+1} = \frac{1}{2} \left(\frac{B_r(\theta, \phi)_{m+2} - B_r(\theta, \phi)_{m+1}}{t_{m+2} - t_{m+1}} + \frac{B_r(\theta, \phi)_{m+1} - B_r(\theta, \phi)_m}{t_{m+1} - t_m} \right)$. Besides, $h_{00}(t') = 2t'^3 - 3t'^2 + 1$, $h_{10}(t') = t'^3 - 2t'^2 + t'$, $h_{01}(t') = -2t'^3 + 3t'^2$ and $h_{11}(t') = t'^3 - t'^2$ are used to normalize the cubic Hermite interpolation formula.

The inner-boundary velocity is defined as the corresponding value at the centroid of the nearest cell in the inner domain and constrained by a predefined speed $V_{BD,max}$. Considering that the average velocity of plasma flow in the area covered by an inner-boundary face is typically less than 1 Km S^{-1} , we further constrain the inner-boundary facial average plasma velocity to not significantly exceed this velocity as below during our simulations.

$$\mathbf{v}_{BC} = \frac{\mathbf{v}_{inner}}{|\mathbf{v}_{inner}|} (\Upsilon_{\mathbf{v}} V_{BD,max} + (1 - \Upsilon_{\mathbf{v}}) |\mathbf{v}_{inner}|), \tag{17}$$

where $\Upsilon_{\mathbf{v}} = 0.5 + 0.5 \cdot \tanh\left(\frac{|\mathbf{v}_{inner}| - V_{BD,max}}{V_{BD,fac}} \cdot \pi\right)$ with $V_{BD,max} = 1 \text{ Km S}^{-1}$ and $V_{BD,fac} = 2 \text{ m S}^{-1}$. Here \mathbf{v}_{inner} refers to the velocity of plasma flow at the centroid of the nearest cell in the inner domain.

Since this model is designed to mimic coronal structures and provide inner-boundary conditions for inner heliosphere models such as EUHFORIA (Poedts, S. et al. 2020; Pomoell & Poedts 2018) or ICARUS (Verbeke et al. 2022), which start from 0.1 AU where the solar wind is supersonic/super-Alfvénic, the outer boundary of this model is set to $25 R_s$. Since this distance is outwards enough to allow the plasma flow to become supersonic/super-Alfvénic, we prescribe the Neumann boundary conditions at the outer boundary (Brchnelova et al. 2022), therefore all the state variables in the ghost cells nearby out boundary are derived from state variables in the inner computational domain. We extrapolate $r^2 B_r$, B_θ , B_ϕ , ρ , u , v , w p and ψ from the outermost cell centers in computational domain to the ghost cells with a zero gradient (Brchnelova et al. 2022; Perri et al. 2022).

4. Numerical results

In this section, the time-evolving coronal model developed in previous sections is employed to mimic the evolution of the coronal structures during CRs 2219 and 2220. These simulations are around the 2019 eclipse which occurred on July 2, 2019, and are driven by about 1300 GONG-zqs magnetograms downloaded at

<https://gong.nso.edu/data/magmap/QR/zqs/> and ranging from 11:00 on June 29, 2019 to 21:00 on August 22, 2019. As mentioned in Subsection 2.2, the initial magnetic fields for the quasi-steady state coronal simulation are achieved from the potential field (PF) model whose bottom boundary condition is specified by the synoptic maps of the radial photospheric magnetic field centered on 11:00 on June 29, 2019. Followed by the quasi-steady state solar coronal simulation, these time-evolving photospheric magnetograms are used to drive the time-evolving coronal simulations from the solar surface to $25 R_s$ during these two CRs in an inertial coordinate system.

In subsection 4.1, we perform both quasi-steady state and time-evolving MHD coronal simulations and compare their simulation results on July 2, 2019, and July 30, 2019, to validate the time-evolving approach. It demonstrates that the simulated results from the quasi-steady state coronal simulations are generally consistent with those calculated by the time-evolving MHD coronal model when configured at the inner boundary by the same magnetogram. However, the timing diagrams of some variables in the time-evolving coronal simulation are obviously different from those derived from the quasi-steady state simulations. Furthermore, in Subsection 4.2, we evaluate the impact of time-step sizes on the time-evolving coronal simulation results. It shows that the time-evolving coronal model with a time-step size of 10 minutes achieves almost the same simulation results as those calculated with a time-step size of 2 minutes, but gains a speedup of approximately $2.23 \times$.

In this paper, all the calculations are performed on the wice cluster of Tier-2 supercomputer infrastructure from Flemish Supercomputer Center (Vlaams Supercomputer Centrum-VSC), the Flanders’ most highly integrated high-performance research computing environment (<https://www.vscenrum.be/>). All the simulations are completed on 1080 CPU cores. The wall-clock time for the time-evolving coronal simulations with time-step sizes of 10 minutes and 2 minutes, covering two CRs, is approximately 17.54 hours and 39.06 hours, respectively. In the following, we present the results of the MHD coronal simulations during CRs 2219 and 2220.

4.1. Time-evolving versus quasi-steady-state coronal simulation results

In this subsection, we present the simulation results obtained from the time-evolving COCONUT coronal model and compare them with the results from the quasi-steady state COCONUT model. We adopt a constant time-step size of 10 minutes during the time-evolving coronal simulation presented here and include a movie to show the evolution of some selected magnetic field lines between the 82-nd and 735-th hours of the time-evolving simulation. We also compare the simulation results with coronal observations and provide a movie to demonstrate the evolution of pB images synthesized from simulation results and viewed from STEREO-A’s perspective. Additionally, we compare the plasma density, radial velocity, and temperature calculated by the time-evolving coronal model at the 82-nd and 735-th hours of the time-evolving simulation with those calculated by the quasi-steady state COCONUT coronal model, constrained by magnetograms at 19:00 on July 2, 2019, and at 00:00 on July 30, 2019, corresponding to the 82-nd and 735-th hours in the time-evolving simulation. Besides, we display timing diagrams of radial velocity, proton number density, and magnetic field strength during a CR period of physical time within some high-density low-speed (HDLS) and low-density high-speed (LDHS) regions simulated by the time-evolving coronal model. We also map the heliologi-

tude in quasi-steady state coronal simulations to a Carrington rotation period of physical time and compare the timing diagrams of selected variables in both the quasi-steady and time-evolving simulations.

In Fig. 2, we compare white-light pB images from 2.5 to 15 R_s that are observed from the outer coronagraph of the Sun Earth Connection Coronal and Heliospheric Investigation (SECCHI) instrument suite (a, b) on board the STEREO-A spacecraft (Frazin et al. 2012; Howard et al. 2008; Kaiser et al. 2008; Thompson et al. 2003; Thompson & Reginald 2008) and the white-light pB images synthesized from the quasi-steady state (c, d) and time-evolving (e, f) coronal simulation results. The left panel demonstrates the pB images observed on July 2, 2019 (a), and synthesized from the simulation result of quasi-steady state simulation constrained by magnetograms at 19:00 on July 2, 2019 (c) and from the simulation result at the 82-th hour of the time-evolving simulation (e). The right panel demonstrates the pB images observed on July 30, 2019 (b), and synthesized from the simulation result of quasi-steady state simulation constrained by magnetograms at 00:00 on July 30, 2019 (d) and from the simulation result at the 735-th hour of the time-evolving simulation (f). The observed and modeled images all show four bright structures near the solar equator. However, the locations of the two simulated bright structures in the northern hemisphere are further north and the simulated bright structure at the southeast limb extends further outward, compared with those in the observation results. This discrepancy may be attributed to inaccurate observations for both polar photospheric magnetic fields. Additionally, it can be seen that there are no obvious differences in both observed and simulated pB images after the corona evolves over a CR period. The pB images synthesized from both quasi-steady state and time-evolving coronal simulations constrained by the same magnetogram also show no significant differences. Besides, we illustrate the simulated magnetic field lines with orange lines on these selected meridians. It demonstrates that the close-field regions are typically accompanied by bright structures. Additionally, interested readers can refer to online movie 1 to see the evolution of simulated pB images observed from the COR2/Stereo-A field of view during the 82-nd and 735-th hours of the time-evolving coronal simulation.

In Fig. 3, we further present the observed white-light pB images at 3 R_s , these images are synthesized from observations during CRs 2219 (a) and 2210 (b) and displayed in the Carrington co-rotating coordinate system. Overlaid on these pB contours are magnetic field neutral lines (MNLs) denoted by yellow solid, yellow dashed, and black solid lines, representing the simulated results calculated by quasi-steady state COCONUT coronal model, PF solver, and time-evolving COCONUT coronal model, respectively. It can be seen that the MNLs calculated in quasi-steady state and time-evolving simulations constrained by the same magnetogram almost coincide with each other. The segments of these MNLs between 240° and 20° in longitude capture the observed bright structures extending more than 15° poleward, which are missed in the MNLs calculated by the PF solver. However, between 20° and 240° in longitude, the segments of these MNLs calculated by MHD models are about 10° northern than those calculated by PF solver and the central axis of these observed bright structures. These discrepancies may be attributed to the fact that certain mechanisms, such as coronal heating and solar acceleration, which can affect magnetic pressure and ultimately impact the distribution of MNLs, are only empirically rather than self-consistently formulated in this MHD coronal model.

In Fig. 4 and Fig. 5, we demonstrate distributions of radial velocity and the proton number density, with the latter scaled by multiplying the dimensionless heliocentric distance. These contours range from 1 to 20 R_s on the same meridians and moments as in Fig. 2 and overlaid on these contours are magnetic field lines denoted by black lines. The results in the top (a, b) and bottom (c, d) panels are calculated by quasi-steady state and time-evolving coronal models, respectively. It is obvious that the high-density low-speed flows are dominated by close-field structures in low-latitude regions, while the low-density high-speed flows occupy the high-latitude regions, accompanied by open-field structures. It is a key characteristic of solar minima. Additionally, minor differences in the magnetic field lines within the closed-field regions can be observed between the quasi-steady state and time-evolving coronal simulations. Also, in the left hemisphere of these selected meridians, regions of low speed less than 50 (Km S^{-1}) and scaled high density larger than 5×10^6 (cm^{-3}) are slightly narrower in the time-evolving simulation compared to the quasi-steady state coronal simulations. These differences may be attributed to the electric field caused by temporal variations in the magnetic field near the inner boundary in the time-evolving coronal simulation. Also, it can be seen that after a CR period of physical time, there are significant differences in the simulated close-field lines in both quasi-steady state and time-evolving simulations. These differences are a consequence of changes in magnetograms, which serve as inner-boundary conditions, in different moments. Additionally, interested readers can refer to online movie 2 to see the evolution of some simulated magnetic field lines in 3D illustration observed in the HCI coordinate system during the 82-nd and 735-th hours of the time-evolving coronal simulation. The continuous formation and disappearance of closed field lines, which cannot be observed in quasi-steady state coronal simulations, is evident during the time-evolving procedure.

In Fig. 6, we present the distribution of radial velocity at 3 (a, b) and 20 R_s (e, f) calculated at the 82-nd (a, e) and 735-th (b, f) hours of the time-evolving coronal simulation. In Fig. 7 and Fig. 8, we show the distribution of the proton number density and plasma temperature on these places and moments as those in Fig. 6. We also display the distribution of relative differences in radial velocity, $\text{RD}_{V_r} = 2 \frac{V_r^{\text{TE}} - V_r^{\text{QSS}}}{V_r^{\text{TE}} + V_r^{\text{QSS}}}$, plasma density, $\text{RD}_\rho = 2 \frac{\rho^{\text{TE}} - \rho^{\text{QSS}}}{\rho^{\text{TE}} + \rho^{\text{QSS}}}$, and plasma temperature, $\text{RD}_T = 2 \frac{T^{\text{TE}} - T^{\text{QSS}}}{T^{\text{TE}} + T^{\text{QSS}}}$, between quasi-steady state and time-evolving coronal simulations, denoted by superscripts “QSS” and “TE”, respectively, at 3 (c, d) and 20 R_s (g, h). Overlaid on these contours are MNLs, denoted by black solid lines for the time-evolving coronal model, white dashed lines for the quasi-steady state coronal model, and white solid lines for the PF solver. It can be seen that the MNLs calculated by MHD models extend more poleward than those calculated by the PF solver. The high-density, low-speed flows primarily span around the MNLs, the distribution pattern of plasma temperature is basically consistent with the distribution pattern of radial velocity, and there are significant differences in the ‘U’-shaped segments of the MNLs calculated by the quasi-steady state and time-evolving coronal models at 20 R_s . Moreover, the largest relative differences in radial velocity, plasma density, and temperature are mainly concentrated around the MNLs. Additionally, the relative differences in these variables calculated by quasi-steady state and time-evolving models at 20 R_s are larger than those at 3 R_s , but they still remain less than 5% in radial velocity, less than 10% in plasma density and less than 8% in plasma density in most regions at 20 R_s .

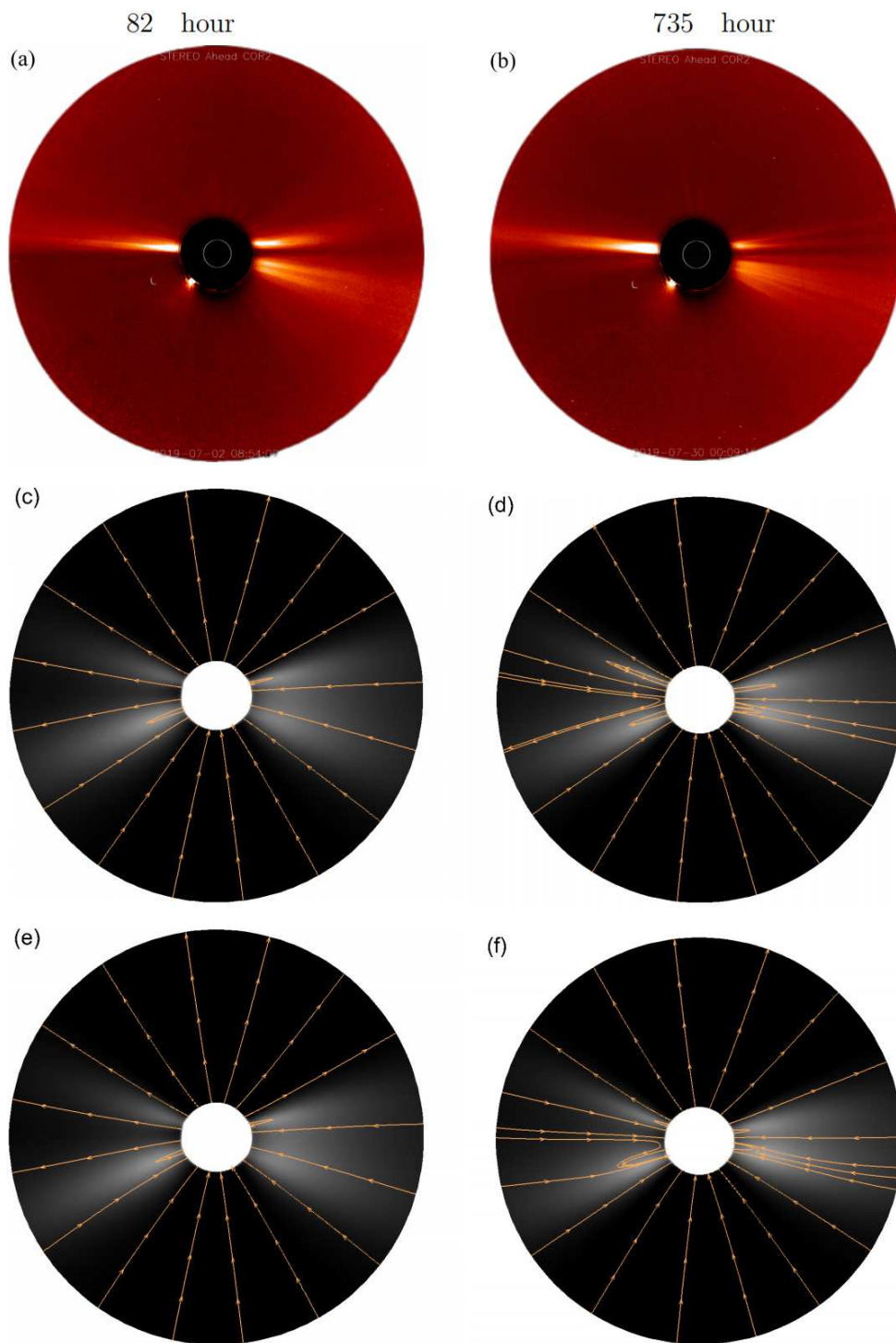


Fig. 2. White-light pB images observed from COR2/STEREO-A on July 2, 2019 (a) and July 30, 2019 (b), corresponding pB images synthesized from quasi-steady state coronal simulation results (c, d) constrained by magnetograms at 19:00 on July 2, 2019 (c) and 00:00 on July 30, 2019 (d), and the corresponding pB images synthesized from simulation results at 82 (e) and 735 (f) hours of the time-evolving coronal simulations. These synthesized images range from 2.5 to 15 R_{\odot} on the meridian planes perpendicular to the STEREO-A line of sight, with the orange lines indicating magnetic field lines on these selected meridians. The evolution of simulated pB images during this time interval is demonstrated in online movie 1.

Table 1. Average relative differences in simulation results calculated by quasi-steady state and time-evolving coronal model.

Parameters	$RD'_{ave,\rho}$	$RD'_{ave, v }$	$RD'_{ave, B }$
t=82 hrs	0.54%	1.06%	4.24%
t=735 hrs	0.50%	1.28%	3.67%

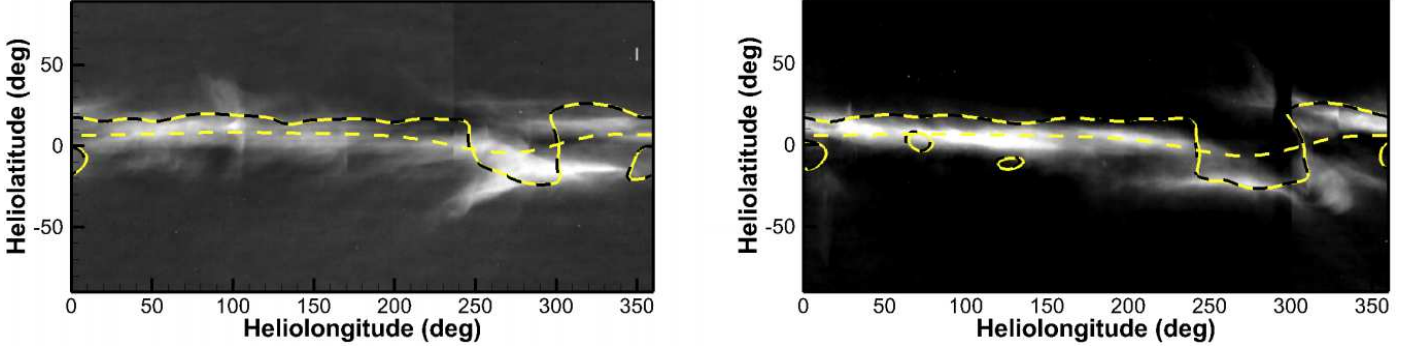


Fig. 3. Synoptic maps of white-light pB observations from SOHO/LASCO C2 at $3 R_s$ for CRs 2219 (a) and 2220 (b). The yellow solid and yellow dashed lines denote the MNLs calculated by the quasi-steady state coronal model and the PF solver constrained by magnetograms at 19:00 on July 2, 2019 (left) and 00:00 on July 30, 2019 (right), and the black solid lines represent the MNLs calculated at the 82-nd (left) and 735-th (right) hours of the time-evolving coronal simulation.

Also, we calculated the average relative differences in plasma density $RD_{ave,\rho}^t$, velocity $RD_{ave,|v|}^t$ and magnetic field $RD_{ave,|B|}^t$ between the simulation results calculated by quasi-steady state and time-evolving coronal simulations. Here $RD_{ave,\rho}^t$, $RD_{ave,|v|}^t$ and $RD_{ave,|B|}^t$ are defined as below,

$$RD_{ave,\rho}^t = \frac{\sum_{i=1}^N |\rho_{i,QSS}^t - \rho_{i,TE}^t|}{0.5 \sum_{i=1}^N (\rho_{i,QSS}^t + \rho_{i,TE}^t)},$$

$$RD_{ave,|v|}^t = \frac{\sum_{i=1}^N |v_{i,QSS}^t - v_{i,TE}^t|}{0.5 \sum_{i=1}^N (v_{i,QSS}^t + v_{i,TE}^t)},$$

$$RD_{ave,|B|}^t = \frac{\sum_{i=1}^N |B_{i,QSS}^t - B_{i,TE}^t|}{0.5 \sum_{i=1}^N (B_{i,QSS}^t + B_{i,TE}^t)}.$$

The superscript “ t ” denotes the corresponding variable calculated at the moment t during the time-evolving simulation, the subscript “ i_{QSS} or TE ” denotes the corresponding variable in cell i calculated by the quasi-steady state and time-evolving coronal models, and N is the number of cells in the computational domain. It can be seen that the overall differences between the simulation plasma densities and velocities calculated by the quasi-steady state and time-evolving coronal models are very small, less than 1.5%, and the average relative difference in magnetic field strength is also less than 4.5%.

In Fig. 9, we display some timing diagrams of radial velocity, proton number density, and magnetic field strength during the 82-nd and 735-th hours of the time-evolving coronal simulation. These timing diagrams are denoted by black solid lines and these parameters are observed by a virtual satellite placed at $(r, \theta, \phi) = (3 R_s, 0, 201^\circ)$ and $(r, \theta, \phi) = (20 R_s, 0, 201^\circ)$, which located in the HDLS region. Additionally, we map the heliolongitude in quasi-steady state coronal simulations to a Carrington rotation period of physical time as below,

$$t = \begin{cases} 82 - 653 \frac{\phi - \phi_0}{360^\circ}, & \text{if } \phi \leq \phi_0 \\ 735 - 653 \frac{\phi - \phi_0}{360^\circ}, & \text{if } \phi > \phi_0 \end{cases},$$

where $\phi_0 = 201^\circ$. The selected variables calculated by the quasi-steady state coronal models, constrained by magnetograms at 19:00 on July 2, 2019 and 00:00 on July 30, 2019, along the mapped time at $(r, \theta) = (3 R_s, 0)$ and $(r, \theta) = (20 R_s, 0)$ are shown by dashed and dash-dot lines, respectively. It demonstrates that the peaks and troughs in the profiles of these timing diagrams in the time-evolving simulation are obviously different from those in the quasi-steady state coronal simulations. The radial velocity and plasma density in the time-evolving coronal simulation are usually between those calculated by the two quasi-steady state coronal simulations. Additionally, the troughs in the timing diagrams of magnetic field strength occur earlier than those calculated by the quasi-steady state coronal model.

Similar to the comparison made in Fig. 10, we further compare the timing diagrams of these selected variables in the LDHS region calculated by both quasi-steady state and time-evolving coronal models in Fig. 10. It demonstrates that the differences between these selected variables calculated by the quasi-steady state and time-evolving coronal models are much more obvious in the LDHS regions compared to the HDLS regions. It can be seen that the peaks and troughs in the profiles of these timing diagrams at $3 R_s$ occur at almost the same moments as those at $20 R_s$ for both the time-evolving and quasi-steady state simulations. However, the peaks and troughs occurring around the 160-th, 220-th, 320-th, and 660-th hours in the profiles calculated by the time-evolving coronal model are not observed in the quasi-steady state simulations.

4.2. The impact of time-step sizes on simulation results

In this subsection, we evaluate the impact of time-step sizes on the time-evolving coronal simulation results. We perform a time-evolving coronal simulation with a constant time-step size of 2 minutes and compare the simulated plasma density, velocity, and magnetic field strength with those from the time-evolving coronal simulation with a time-step size of 10 minutes mentioned above. Also, we provide some movies to show the temporal evolution of the differences in some of these variables between the two time-evolving coronal simulations with different time-step sizes.

In the time-evolving coronal simulation with a time-step size of 10 minutes, approximately 7 to 9 Newtonian iterations, as described in Subsection. (3.1), are typically performed in each time step. However, there are a few time steps where the L_2 norm

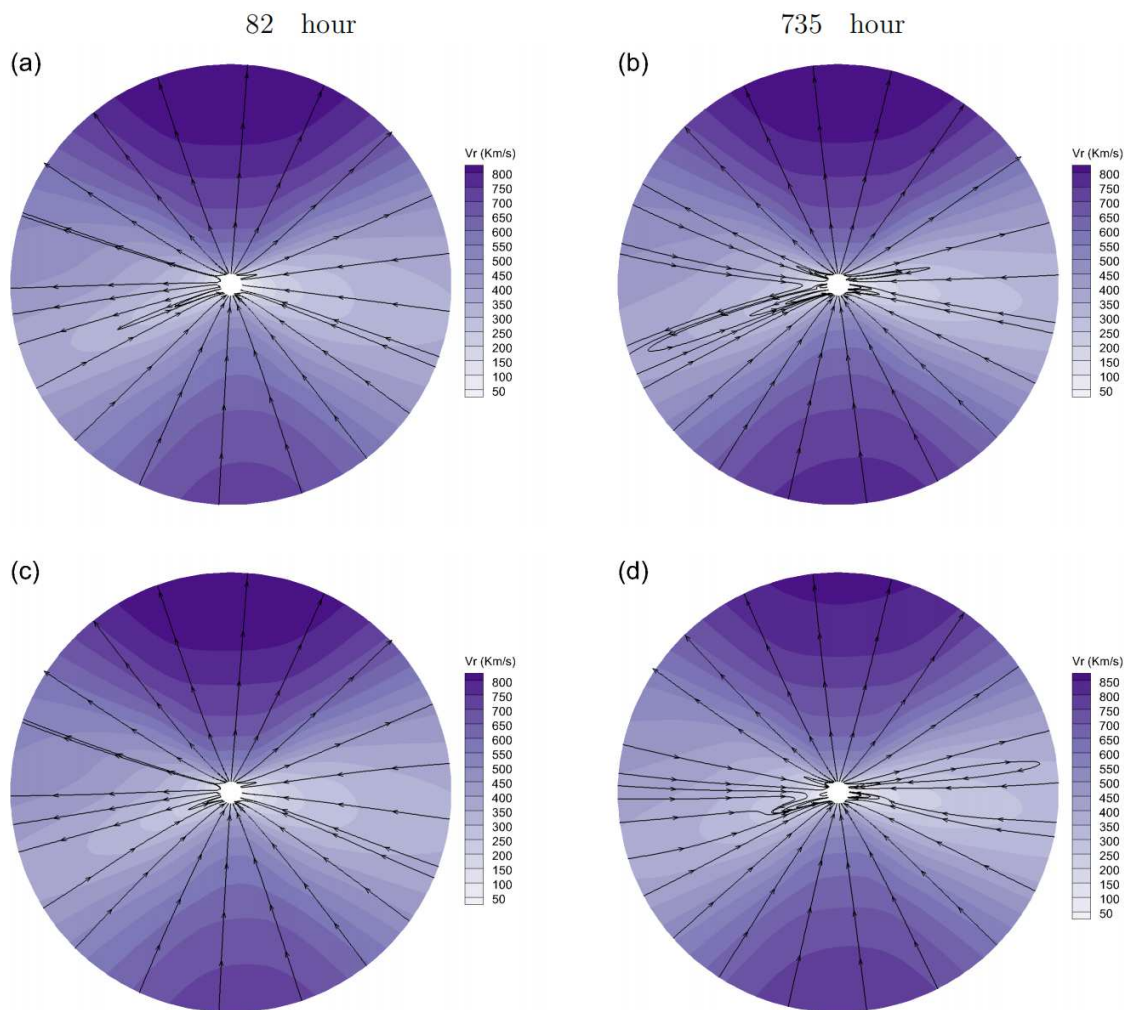


Fig. 4. Magnetic field lines from 1 to $20 R_s$ overlaid on contours of the radial plasma speeds V_r (Km S^{-1}) on the meridian planes perpendicular to the STEREO-A line of sight. The top panel denotes quasi-steady state simulation results constrained by magnetograms at 19:00 on July 2, 2019 (a) and 00:00 on July 30, 2019 (b), the bottom panel represents simulation results at the 82-nd (c) and 735-th (d) hours of the time-evolving coronal simulation. Evolution of some selected magnetic field in 3D dimension during this time interval is illustrated in online movie 2.

of the differences between the state variables updated in two consecutive Newton iterations fluctuates around a value larger than the threshold used to stop the Newtonian iterations. In such cases, we terminate the Newton iterations at the 10-th iteration. In the time-evolving simulation with a time-step size of 2 minutes, approximately 5 to 6 Newtonian iterations are typically performed in each time step, and the computational time is about 2.23 times as this in the time-evolving simulation with a time-step size of 10 minutes.

In Fig. 11, we present the distributions of the relative differences in plasma density (a, b) and absolute differences in radial velocity (c, d) between the results calculated with time-step sizes of 2 and 10 minutes, ranging from 1 to $20 R_s$ on the same meridians and moments as in Fig. 2. It demonstrates that the relative differences in plasma density are less than 0.2% and the absolute differences in radial velocity are less than 0.5 Km S^{-1} in most regions. Overlaid on these contours are magnetic field lines denoted by black lines. It can be found that the largest absolute differences in radial velocity mainly occur in open-field regions, while the largest relative differences in plasma density occur in both open- and close-field regions.

In Fig. 12, we show the relative differences in plasma density (a, b, e, f) and radial velocity (c, d, g, h) between the results calculated with time-step sizes of 2 and 10 minutes at 3 (a, b, c, d) and $20 R_s$ (e, f, g, h). Overlaid on these contours are MNLs calculated from these two time-evolving simulations. It can be seen that the MNLs calculated with a time-step size of 10 and 2 minutes, denoted by orange dashed and black solid lines respectively, are coincided with each other at both 3 and $20 R_s$. Additionally, the relative differences in plasma density and radial velocity are less than 0.2% and 0.1%, which are extremely small, in most regions. Besides, it can be found the largest relative differences mainly distributed around the MNLs. Additionally, interested readers can refer to the online movies 3 and 4 to see the evolution of MNLs overlaid on relative differences in magnetic field strength at 3 and $20 R_s$, respectively. These movies demonstrate that the relative differences in magnetic field strength are less than 3% and 6% in most regions at 3 and $20 R_s$ during the time-evolving simulations, and the largest relative differences mainly distribute around the MNLs.

In Fig. 13, we illustrate the timing diagrams of radial velocity, proton number density, and magnetic field strength within the HDLS flow region, calculated with a time-step size of 10 (black

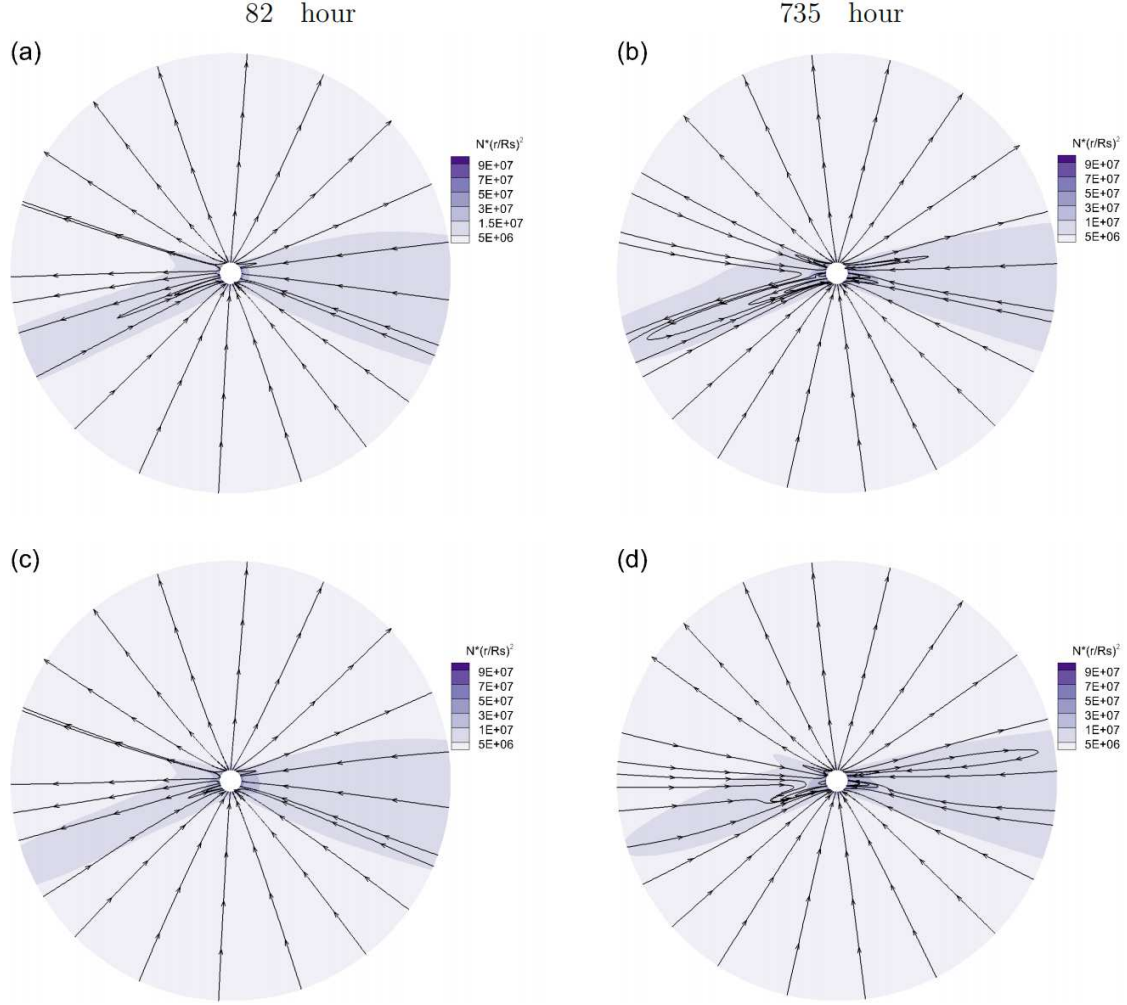


Fig. 5. Magnetic field lines from 1 to $20 R_s$ overlaid on contours of the proton number density N (cm^{-3}), multiplied by the dimensionless heliocentric distance $\left(\frac{r}{R_s}\right)^2$, on the same meridian planes as in Fig. 4.

solid lines) and 2 minutes (orange dashed lines). It demonstrates that these variables calculated with time-step sizes of 10 minutes and 2 minutes are generally the same during the time-evolving simulations, except for some minor differences in magnetic field strength at $20 R_s$ between 440 and 470 hours and between 490 and 620 hours.

In Fig. 14, we further demonstrate the timing diagrams of these selected variables within the LDHS flow region, calculated with a time-step size of 10 (black solid lines) and 2 minutes (orange dashed lines). It can be seen that the radial velocity and proton number density calculated with time-step sizes of 10 minutes and 2 minutes are still generally the same during the time-evolving simulations at both $3 R_s$ and $20 R_s$. The magnetic field strength calculated with time-step sizes of 10 minutes and 2 minutes is essentially the same at $3 R_s$ during the time-evolving simulations. However, the magnetic field strength at $20 R_s$ calculated with a time-step size of 2 minutes exhibits fluctuations around the value obtained with a time-step size of 10 minutes during these two time-evolving simulations. This fluctuation may be attributed to the impact of the additional magnetograms interpolated with a time-step size of 2 minutes, which do not appear in the simulation with the larger time-step size of 10 minutes. Although there is a fluctuation in magnetic field

strength at $20 R_s$ calculated with a smaller time-step size compared to a larger time-step size, the magnitude of this fluctuation is less than 5% relative to the corresponding magnetic field strength and it hardly affects the other simulated state variables.

Additionally, in Table 2, we list the average relative differences in plasma density $\text{RD}_{\text{ave},\rho}^t$, velocity $\text{RD}_{\text{ave},|\mathbf{v}|}^t$ and magnetic field $\text{RD}_{\text{ave},|\mathbf{B}|}^t$ between the simulation results calculated with time-step sizes of 2 and 10 minutes, and the wall-clock time required in both time-evolving coronal simulations. $\text{RD}_{\text{ave},\rho}^t$, $\text{RD}_{\text{ave},|\mathbf{v}|}^t$ and $\text{RD}_{\text{ave},|\mathbf{B}|}^t$ are defined as below,

$$\text{RD}_{\text{ave},\rho}^t = \frac{\sum_{i=1}^N |\rho_{i,\text{dt}=2 \text{ min}}^t - \rho_{i,\text{dt}=10 \text{ min}}^t|}{0.5 \sum_{i=1}^N (\rho_{i,\text{dt}=2 \text{ min}}^t + \rho_{i,\text{dt}=10 \text{ min}}^t)},$$

$$\text{RD}_{\text{ave},|\mathbf{v}|}^t = \frac{\sum_{i=1}^N |\mathbf{v}_{i,\text{dt}=2 \text{ min}}^t - \mathbf{v}_{i,\text{dt}=10 \text{ min}}^t|}{0.5 \sum_{i=1}^N |\mathbf{v}_{i,\text{dt}=2 \text{ min}}^t + \mathbf{v}_{i,\text{dt}=10 \text{ min}}^t|},$$

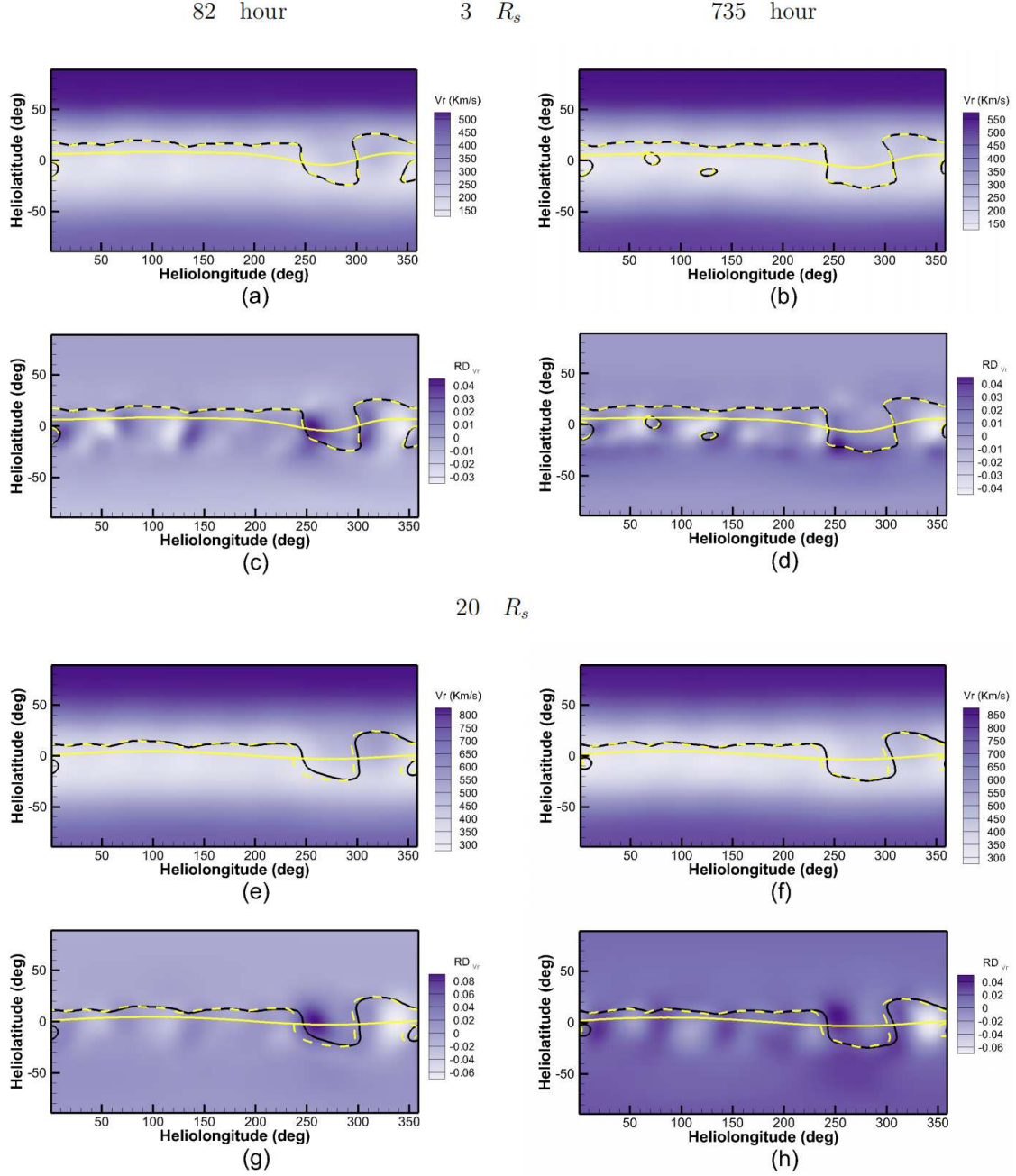


Fig. 6. Synoptic maps of the radial plasma speeds V_r in unit of Km S^{-1} (a, b, e, f) calculated by the time-evolving coronal model, and the relative differences in plasma velocity between quasi-steady state and time-evolving coronal simulations (c, d, g, h) at $3 R_s$ (a, b, c, d) and $20 R_s$ (e, f, g, h). The left and right panels represent simulation results at the 82-nd and 735-th hours of time evolving coronal simulation, or corresponding to the quasi-steady state coronal simulation results constrained by magnetograms at 19:00 on July 2, 2019, and 00:00 on July 30, 2019. The black solid lines denote the MNLs calculated by the time-evolving coronal model, and the white dashed and white solid lines represent the MNLs calculated by the quasi-steady state coronal model and the PF solver.

$$RD_{\text{ave},|\mathbf{B}|}^t = \frac{\sum_{i=1}^N |\mathbf{B}'_{i,\text{dt}=2 \text{ min}} - \mathbf{B}'_{i,\text{dt}=10 \text{ min}}|}{0.5 \sum_{i=1}^N |\mathbf{B}'_{i,\text{dt}=2 \text{ min}} + \mathbf{B}'_{i,\text{dt}=10 \text{ min}}|}.$$

Here the superscript “ t ” denotes the corresponding variable calculated at the moment t during the time-evolving simulation, the subscript “ $_{i,\text{dt}=\chi}$ ” denotes the corresponding variable in cell i calculated by the time-evolving coronal model with a time-step size of $\text{dt} = \chi$, and N is the number of cells in the computational do-

main. It can be seen that the overall differences between the simulation results calculated with $\text{dt} = 10 \text{ min}$ and $\text{dt} = 2 \text{ min}$ are very small, less than 1%, whereas the computational time with $\text{dt} = 2 \text{ min}$ is almost 2.23 times as long as that with $\text{dt} = 10 \text{ min}$. It demonstrates that the computational efficiency of the implicit time-evolving coronal model can be improved by increasing the time-step size, while still maintaining the required temporal accuracy.

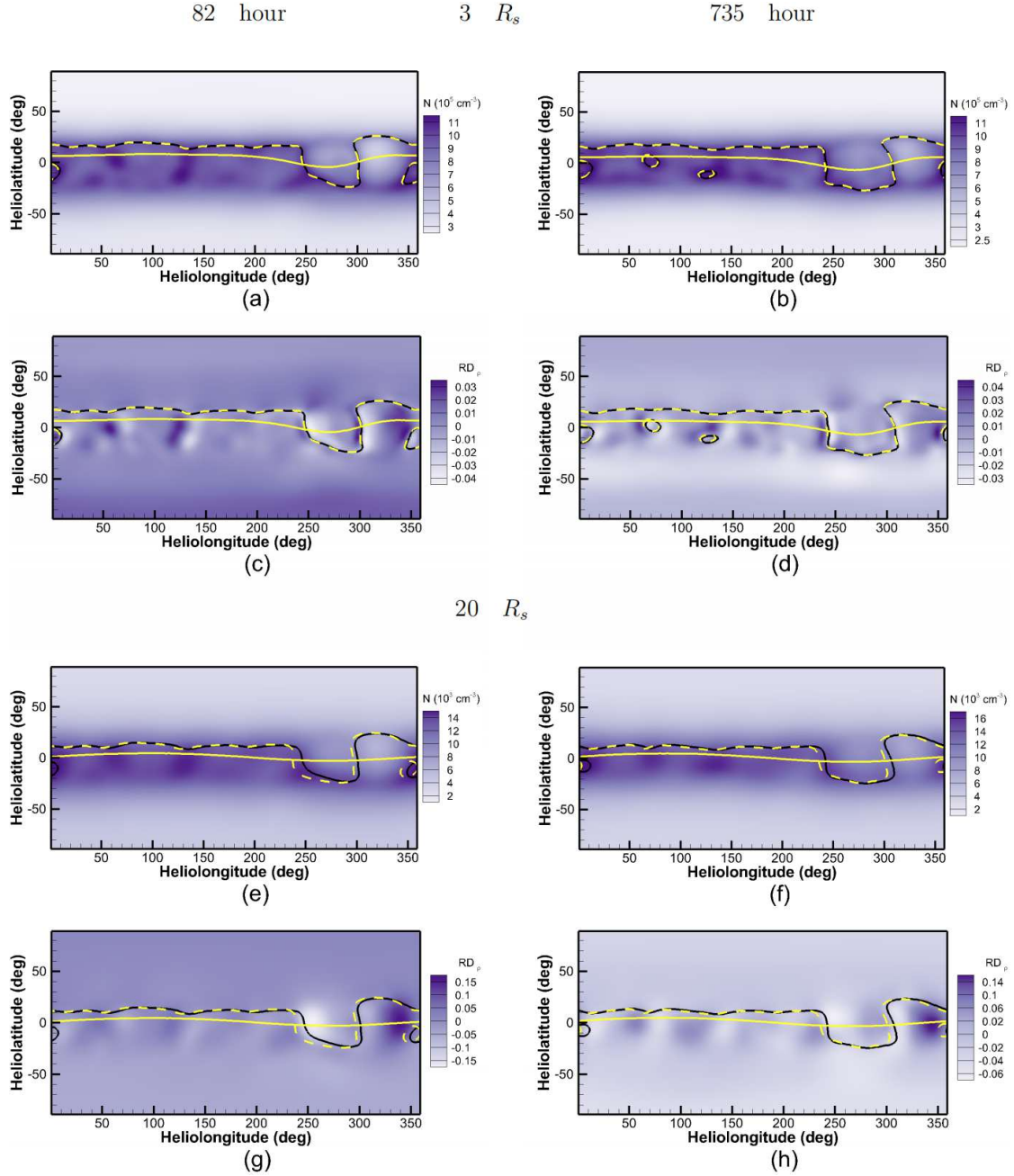


Fig. 7. Synoptic maps of the proton number density N in units of 10^5 cm^{-3} (a, b) and 10^3 cm^{-3} (e, f) calculated by the time-evolving coronal model, and the relative differences in proton number density between quasi-steady state and time-evolving coronal simulations (c, d, g, h). The locations, moments and lines in these panels are the same as those in Fig. 6.

Table 2. Comparison of time-evolving coronal simulations with $dt = 10$ and 2 minutes, for 2 Carrington Rotations of physical time.

wall-clock time (hrs)	$RD_{\text{ave},\rho}^{82 \text{ hrs}}$ & $RD_{\text{ave},\rho}^{735 \text{ hrs}}$	$RD_{\text{ave}, v }^{82 \text{ hrs}}$ & $RD_{\text{ave}, v }^{735 \text{ hrs}}$	$RD_{\text{ave}, B }^{82 \text{ hrs}}$ & $RD_{\text{ave}, B }^{735 \text{ hrs}}$
39.06 & 17.54 for $dt=2$ & 10 min	0.09% & 0.08%	0.10% & 0.09%	0.60% & 0.42%

5. Concluding remarks

Steady-state coronal models are constrained by a time-invariant magnetogram and aim to achieve a steady-state coronal structure. Time-dependent coronal models must be time-accurate to capture dynamic features of the corona, such as the propagation of CMEs. Time-evolving coronal models, which are both

time-accurate and driven by more realistic time-evolving magnetograms, can capture the time-evolving features of the corona with higher fidelity.

In this paper, we extend the recently developed time-dependent COCONUT coronal model to a time-evolving coronal model. It is the first fully implicit time-evolving MHD coro-

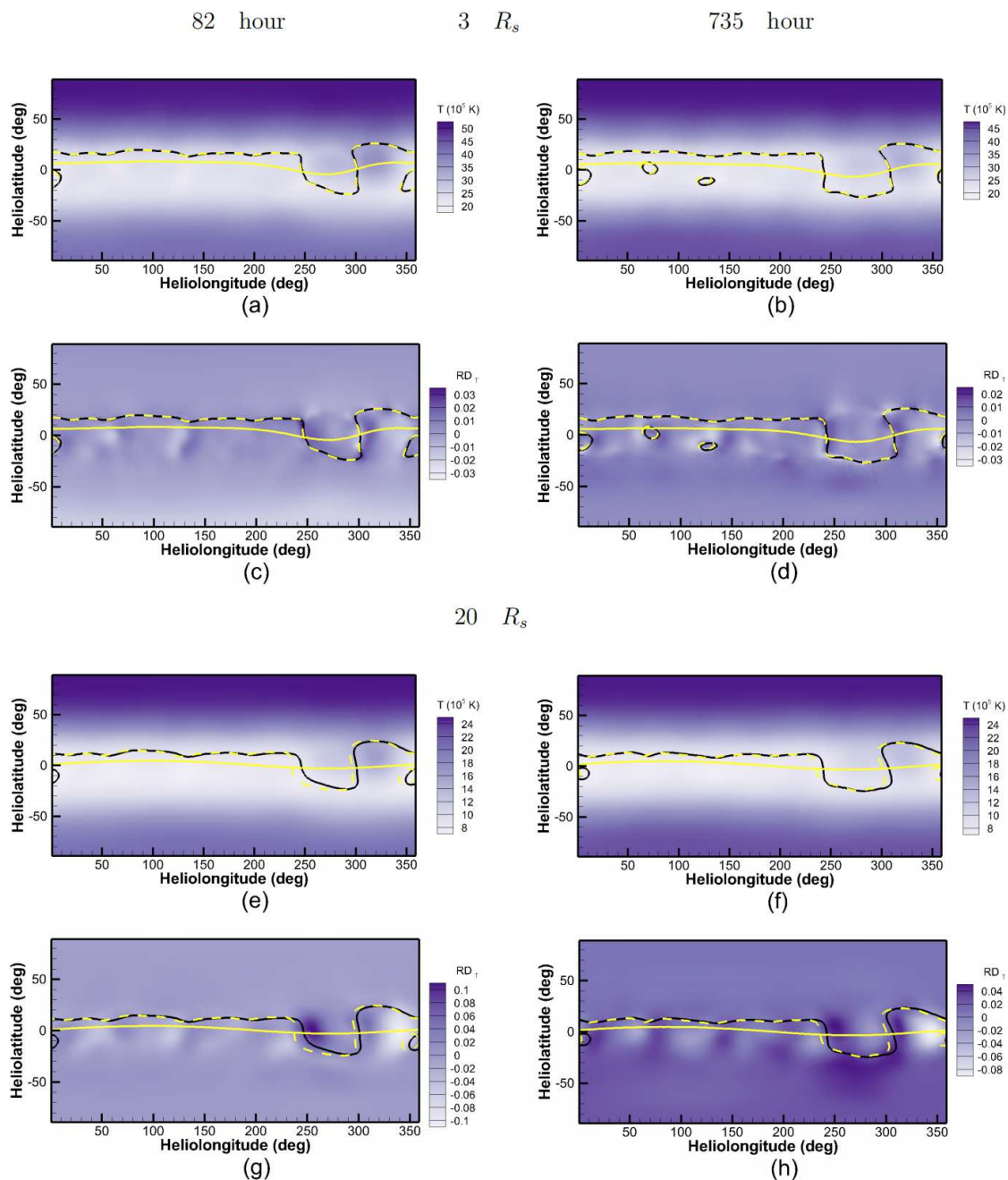


Fig. 8. Synoptic maps of the plasma temperature T in unit of 10^5 K (a, b, e, f) and the relative differences in plasma temperature between quasi-steady state and time-evolving coronal simulations (c, d, g, h). The locations, moments, and lines in these panels are the same as those in Fig. 6.

nal model. The main advantage of this time-evolving coronal model is its flexibility in selecting time-step sizes without being entirely constrained by the Courant-Friedrichs-Lewy (CFL) stability restriction. This feature allows us to enhance computational efficiency by increasing the time-step sizes during the time-evolving coronal simulation. Also, we design an HLL Riemann solver with a self-adjustable dissipation term, which reduces the dissipation term by half for low-speed flows and reverts to the original one for high-speed flows. It makes the solver perform well in solving both incompressible low-speed and compressible high-speed flows and improves the numerical stability of our coronal model in these simulations. Additionally, during the time-evolving coronal simulations, we appropriately ad-

justed the plasma density to avoid the abnormally large Alfvénic speed in the computational domain. It enhances the PP property of this COCONUT coronal model.

We use a series of hourly updated GONG-zqs magnetograms to drive this time-evolving coronal model, mimicking the evolution of dynamic coronal structures from the solar surface to 0.1 AU during two CRs around the 2019 eclipse in an inertial coordinate system. This time-evolving coronal model successfully reproduces some observed coronal structures, such as those seen in pB images. We also compare the results in the time-evolving coronal simulation driven by time-evolving magnetograms with the quasi-steady state coronal simulations constrained by a time-invariant magnetogram. This comparison val-

updates the time-evolving coronal model with a large time-step size. It demonstrates that the time-evolving coronal model with a time-step size of 10 minutes can generate coronal structures similar to those calculated by the quasi-steady state coronal model at the moment when their inner boundaries are configured by the same magnetogram. The average relative differences in plasma density, velocity, and magnetic field strength between the time-evolving and quasi-steady state coronal simulations, when configured with the same magnetogram at the inner boundary, are less than 0.6%, 1.3% and 4.3%, respectively. It also shows that the timing diagrams of the state variables simulated by the time-evolving coronal model are obviously different from those derived from the quasi-steady state coronal simulations by assuming the coronal structures remain unchanged during a CR period. Consequently, we can conclude that during solar minimum, each time step of the time-evolving coronal simulation with a large time step of 10 minutes produces results comparable to those of the steady-state coronal simulation constrained by the same magnetogram, which typically requires thousands of iterations. Additionally, throughout the entire time-evolving coronal simulation, the time-evolving coronal model with a large time step can also capture the temporal evolution of the state variable, which can't be done in the quasi-steady state coronal simulations.

Furthermore, we compare the time-evolving simulation results calculated with a time-step size of 10 and 2 minutes to evaluate the effect of time steps on the simulation results. The comparison demonstrates that the relative differences in the state variables calculated with a time-step size of 10 and 2 minutes are very small. The average relative differences in plasma density, velocity, and magnetic field strength between the simulations with different time-step sizes are no more than 0.09%, 0.10%, and 0.60%, respectively. However, the computational time with a time-step size of 10 minutes is no more than half of that required for simulation with a time-step size of 2 minutes. We can conclude that the computational efficiency of the fully implicit time-evolving coronal model can be significantly improved by increasing the time-step size, while still maintaining the required temporal accuracy.

Considering that the computational time of 1281 hours of physical time is no more than 18 hours when adopting a time-step size of $dt = 10$ min, it is practical to adopt a smaller dt to obtain more accurate simulation results for high-frequency events such as CMEs, at the expense of an acceptable reduction in computation efficiency. In fact, we can adjust the physical time-step size according to the temporal accuracy required for our specific research or practical application, thereby further optimizing time-step sizes to simultaneously maintain high efficiency and the necessary numerical stability and accuracy.

Although this established fully implicit time-evolving MHD solar coronal model is merited in many aspects and acts as a promising tool to timely and accurately simulate the time-evolving corona in practical space weather forecasting, there is still some room for further improvement. In our future work, we will try to couple this highly efficient time-evolving coronal model with an inner heliosphere model such as EUHFORIA to further validate its ability to improve the performance of the current Sun-to-Earth model chain in providing timely and accurate space weather forecasting. Additionally, we will attempt to use some surface flux transport models such as the Advective Flux Transport (AFT) model (Upton & Hathaway 2014) to advect the radial magnetic field with observed flows. This may help us produce a more realistic magnetic field evolution at the inner boundary of our coronal model. Furthermore, we may also try

to incorporate additional observations into the inner boundary conditions, such as inferring horizontal velocities from observational data using the time-distance helioseismology method. (Yalim et al. 2017; Zhao et al. 2012). Besides, further decreasing the magnetic field discretization error by solving decomposed MHD equations (e.g., Feng et al. 2010; Li et al. 2018; Wang et al. 2019a) may stabilize COCONUT numerically even when dealing with extremely low- β problems.

Acknowledgements. This work is also part of a project supported by the Specialized Research Fund for State Key Laboratories, which is managed by the Chinese State Key Laboratory of Space Weather. The resources and services used in this work were provided by the VSC (Flemish Supercomputer Centre), funded by the Research Foundation – Flanders (FWO) and the Flemish Government. F.Z. is supported by the Research Council of Norway through its Centres of Excellence scheme, project No. 262622. This work utilizes data obtained by the Global Oscillation Network Group (GONG) program, managed by the National Solar Observatory and operated by AURA, Inc., under a cooperative agreement with the National Science Foundation. The data were acquired by instruments operated by the Big Bear Solar Observatory, High Altitude Observatory, Learmonth Solar Observatory, Udaipur Solar Observatory, Instituto de Astrofísica de Canarias, and Cerro Tololo Inter-American Observatory. The authors also acknowledge the use of the STEREO/SECCHI data produced by a consortium of the NRL (US), LMSAL (US), NASA/GSFC (US), RAL (UK), UBHAM (UK), MPS (Germany), CSL (Belgium), IOTA (France), and IAS (France).

References

- Arge, C. N., Odstrcil, D., Pizzo, V. J., & Mayer, L. R. 2003, *AIP Conf. Proc.*, 679, 190
- Aschwanden, M. J. 2005, *Physics of the Solar Corona. An Introduction with Problems and Solutions* (2nd edition) (Verlag Berlin Heidelberg New York: Springer)
- Baker, D. N. 1998, *Adv. Space Res.*, 22, 7
- Balsara, D. S. 2012, *J. Comput. Phys.*, 231, 7504
- Baratashvili, T., Brchnelova, M., Linan, L., Lani, A., & Poedts, S. Submitted, A & A
- Barth, T. J. 1993, in 31st Aerospace Sciences Meeting, aIAA 1993-668
- Brchnelova, M., Kuřma, B., Perri, B., Lani, A., & Poedts, S. 2022, *ApJS*, 263, 18
- Brchnelova, M., Kuřma, B., Zhang, F., et al. 2023, *Sun Geosph.*, 15, 59
- Brchnelova, M., Zhang, F., Leitner, P., et al. 2022, *J. Plasma Phys.*, 88, 905880205
- Burlaga, L. F. 1984, *Space Sci. Rev.*, 39, 255
- Caplan, R. M., Linker, J. A., Mikić, Z., et al. 2019, *J. Phys.: Conf. Ser.*, 1225, 012012
- Caplan, R. M., Mikić, Z., Linker, J. A., & Lionello, R. 2017, *J. Phys.: Conf. Ser.*, 837, 012016
- Cash, M. D., Biesecker, D. A., Pizzo, V., et al. 2015, *Space Weather*, 13, 611
- Dedner, A., Kemm, F., Kröner, D., et al. 2002, *J. Comput. Phys.*, 175, 645
- Dere, K. P., Del Zanna, G., Young, P. R., Landi, E., & Sutherland, R. S. 2019, *ApJS*, 241, 22
- Detman, T., Smith, Z., Dryer, M., et al. 2006, *J. Geophys. Res.: Space Phys.*, 111, A07102
- DeVore, C. R., Boris, J. P., & Sheeley, N. R., Jr. 1984, *Sol. Phys.*, 92, 1
- Downs, C., Roussev, I. I., van der Holst, B., et al. 2010, *ApJ*, 712, 1219
- Dryer, M. 2007, *Asian J. Phys.*, 16, 97
- Einfeldt, B., Munz, C. D., Roe, P. L., & Sjogreen, B. 1991, *J. Comput. Phys.*, 92, 273
- Esquivel, A., Raga, A. C., Cantó, J., et al. 2010, *ApJ*, 725
- Feng, X. S. 2020a, in *Magnetohydrodynamic Modeling of the Solar Corona and Heliosphere*, 125–337
- Feng, X. S. 2020b, *Magnetohydrodynamic Modeling of the Solar Corona and Heliosphere* (Singapore: Springer)
- Feng, X. S., Jiang, C. W., Xiang, C. Q., Zhao, X. P., & Wu, S. T. 2012a, *ApJ*, 758, 62
- Feng, X. S., Li, C. X., Xiang, C. Q., et al. 2017, *ApJS*, 233, 10
- Feng, X. S., Liu, X. J., Xiang, C. Q., Li, H. C., & Wei, F. S. 2019, *ApJ*, 871, 226
- Feng, X. S., Lv, J. K., Xiang, C. Q., & Jiang, C. W. 2023, *Mon. Not. R. Astron. Soc.*, 519, 6297
- Feng, X. S., Wang, H. P., Xiang, C. Q., et al. 2021, *ApJS*, 257, 34
- Feng, X. S., Xiang, C. Q., & Zhong, D. K. 2011a, *Sci Sin-Terrae*, 41, 1
- Feng, X. S., Xiang, C. Q., & Zhong, D. K. 2013a, *Sci Sin-Terrae*, 43, 912

- Feng, X. S., Xiang, C. Q., Zhong, D. K., et al. 2014a, *Comput. Phys. Commun.*, 185, 1965
- Feng, X. S., Yang, L. P., Xiang, C. Q., et al. 2012b, *Sol. Phys.*, 279, 207
- Feng, X. S., Yang, L. P., Xiang, C. Q., et al. 2010, *ApJ*, 723, 300
- Feng, X. S., Zhang, M., & Zhou, Y. F. 2014b, *ApJS*, 214, 6
- Feng, X. S., Zhang, S. H., Xiang, C. Q., et al. 2011b, *ApJ*, 734, 50
- Feng, X. S., Zhong, D. K., Xiang, C. Q., & Zhang, Y. 2013b, *Sci. China Earth Sci.*, 56, 1864
- Feng, X. S., Zhou, Y. F., & Wu, S. T. 2007, *ApJ*, 655, 1110
- Fisher, G. H., Kazachenko, M. D., Welsch, B. T., et al. 2020, *ApJS*, 248, 2
- Fränz, M. & Harper, D. 2002, *Planet. Space Sci.*, 50, 217
- Frazin, R. A., Vásquez, A. M., Thompson, W. T., et al. 2012, *Sol. Phys.*, 280, 273
- Godunov, S. K. 1959, *Mat. Sb. (N.S.)*, 1959, 271
- Gombosi, T. I., Van der Holst, B., Manchester, W. B., & Sokolov, I. V. 2018, *Living Rev. Sol. Phys.*, 15, 4
- Goodrich, C., Sussman, A., Lyon, J., Shay, M., & Cassak, P. 2004, *J. Atmos. Sol.-Terr. Phys.*, 66, 1469, towards an Integrated Model of the Space Weather System
- Guo, J. H., Linan, L., Poedts, S., et al. 2023, *A & A*
- Gurski, K. F. 2004, *SIAM. J. Sci. Comput.*, 25, 2165
- Hayashi, K. 2005, *ApJS*, 161, 480
- Hayashi, K. 2012, *J. Geophys. Res.: Space Phys.*, 117
- Hayashi, K., Abbott, W. P., Cheung, M. C. M., & Fisher, G. H. 2021, *ApJS*, 254, 1
- Hayashi, K., Benevolenskaya, E., Hoeksema, T., Liu, Y., & Zhao, X. P. 2006, *ApJ*, 636, L165
- Hoeksema, J. T., Abbott, W. P., Bercik, D. J., et al. 2020, *ApJS*, 250, 28
- Hollweg, J. V. 1978, *Rev. Geophys.*, 16, 689
- Howard, R. A., Moses, J. D., Vourlidas, A., et al. 2008, *Space Sci. Rev.*, 136, 67
- Jin, M., Manchester, W. B., van der Holst, B., et al. 2017, *ApJ*, 834, 173
- Kaiser, M. L., Kucera, T. A., Davila, J. M., et al. 2008, *Space Sci. Rev.*, 136, 5
- Karypis, G. 2011, in *Encyclopedia of Parallel Computing*, ed. D. Padua (Boston, MA: Springer US), 1117–1124
- Kitamura, K. 2020, in *Advancement of Shock Capturing Computational Fluid Dynamics Methods: Numerical Flux Functions in Finite Volume Method*, 21–67
- Kitamura, K. & Balsara, D. 2018, *Shock Waves*, 29
- Kitamura, K., Shima, E., Fujimoto, K., & Wang, Z. J. 2011, *Commun. Comput. Phys.*, 10, 90
- Koskinen, H. E. J., Baker, D. N., Balogh, A., et al. 2017, *Space Sci. Rev.*, 212, 1137
- Kuźma, B., Brchnelova, M., Perri, B., et al. 2023, *ApJ*, 942, 31
- Lani, A. 2008, PhD thesis, von Karman Institute for Fluid Dynamics
- Li, C. X., Feng, X. S., Xiang, C. Q., et al. 2018, *ApJ*, 867, 42
- Li, H. C. & Feng, X. S. 2018, *J. Geophys. Res.: Space Phys.*, 123, 4488
- Li, H. C., Feng, X. S., & Wei, F. S. 2020, *J. Space Weather Space Clim.*
- Li, H. C., Feng, X. S., & Wei, F. S. 2021, *J. Geophys. Res.: Space Phys.*, 126, e2020JA028870
- Linan, L., Regnault, F., Perri, B., et al. 2023, *A & A*, 675, A101
- Linker, J. A., Caplan, R. M., Downs, C., et al. 2016, *J. Phys.: Conf. Ser.*, 719, 012012
- Lionello, R., Downs, C., Mason, E. I., et al. 2023, *ApJ*, 959, 77
- Lionello, R., Linker, J. A., & Mikić, Z. 2008, *ApJ*, 690, 902
- Lugaz, N. & Roussev, I. 2011, *J. Atmos. Sol.-Terr. Phys.*, 73, 1187, three dimensional aspects of CMEs, their source regions and interplanetary manifestations
- Mason, E. I., Lionello, R., Downs, C., et al. 2023, *ApJL*, 959, L4
- McCrea, I. W. & Rae, J. 2019, in *ESA Voyage 2050 White Paper*
- Merkin, V. G., Lyon, J. G., Lario, D., Arge, C. N., & Henney, C. J. 2016, *J. Geophys. Res.: Space Phys.*, 121, 2866
- Mignone, A., Bodo, G., Massaglia, S., et al. 2007, *ApJS*, 170, 228
- Mikić, Z., Linker, J. A., Schnack, D. D., Lionello, R., & Tarditi, A. 1999, *Phys. Plasmas*, 6, 2217
- Minoshima, T., Kitamura, K., & Miyoshi, T. 2020, *ApJS*, 248, 12
- Minoshima, T. & Miyoshi, T. 2021, *J. Comput. Phys.*, 446, 110639
- Mok, Y., Mikić, Z., Lionello, R., & Linker, J. A. 2005, *ApJ*, 621, 1098
- Nakamizo, A., Tanaka, T., Kubo, Y., et al. 2009, *J. Geophys. Res.: Space Phys.*, 114
- Odstreil, D., Pizzo, V. J., Linker, J. A., et al. 2004, *J. Atmos. Sol.-Terr. Phys.*, 66, 1311, towards an Integrated Model of the Space Weather System
- Owens, M. J., Lockwood, M., & Riley, P. 2017, *Sci Rep*, 7, 41548
- Parker, E. N. 1963, *Interplanetary dynamical processes* (New York: Interscience Publishers)
- Perri, B., Brun, A. S., Réville, V., & Strugarek, A. 2018, *J. Plasma Phys.*, 84
- Perri, B., Kuźma, B., Brchnelova, M., et al. 2023, *ApJ*, 943, 124
- Perri, B., Leitner, P., Brchnelova, M., et al. 2022, *ApJ*, 936, 19
- Poedts, S., Lani, A., Scolini, C., et al. 2020, *J. Space Weather Space Clim.*, 10, 57
- Pomoell, J. & Poedts, S. 2018, *J. Space Weather Space Clim.*, 8, A35
- Réville, V., Velli, M., Panasenco, O., et al. 2020, *ApJS*, 246, 24
- Riley, P., Linker, J. A., Lionello, R., & Mikić, Z. 2012, *J. Atmos. Sol.-Terr. Phys.*, 83, 1
- Rosner, R., Tucker, W., & Vaiana, G. 1978, *ApJ*, 220
- Samara, E., Pinto, R. F., Magdalení, J., et al. 2021, *A & A*, 648, A35
- Sauerwein, H. S. 1966, *J. Fluid Mech.*, 25, 17–41
- Schrijver, C. & DeRosa, M. 2003, *Sol. Phys.*, 212, 165
- Shen, F., Liu, Y. S., & Yang, Y. 2021, *ApJS*, 253, 12
- Singer, H. J., Heckman, G. R., & Hirman, J. W. 2001, *Space Weather Forecasting: A Grand Challenge* (Washington, DC: American Geophysical Union (AGU)), 23–29
- Siscoe, G. 2000, *J. Atmos. Sol.-Terr. Phys.*, 62, 1223
- Sokolov, I. V., van der Holst, B., Manchester, W. B., et al. 2021, *ApJ*, 908, 172
- Srivastava, A. K., Erdélyi, R., Poedts, S., Chen, P. F., & Yan, Y. H. 2021, *Front. Astron. Space Sci.*, 8
- Thompson, W. & Reginald, N. 2008, *Sol. Phys.*, 250, 443
- Thompson, W. T., Davila, J. M., Fisher, R. R., et al. 2003, in *SPIE Astronomical Telescopes + Instrumentation*
- Tóth, G., De Zeeuw, D. L., Gombosi, T. I., & Powell, K. G. 2006, *Journal of Computational Physics*, 217, 722
- Tóth, G., Ma, Y. J., & Gombosi, T. I. 2008, *J. Comput. Phys.*, 227, 6967–6984
- Tóth, G., van der Holst, B., Sokolov, I. V., et al. 2012, *J. Comput. Phys.*, 231, 870
- Upton, L. & Hathaway, D. H. 2014, *ApJ*, 780, 5
- Usmanov, A. V. 1993, *Sol. Phys.*, 146, 377
- Usmanov, A. V. & Goldstein, M. L. 2003, *AIP Conf. Proc.*, 679, 393
- van der Holst, B., Huang, J., Sachdeva, N., et al. 2022, *ApJ*, 925, 146
- van der Holst, B., Sokolov, I. V., Meng, X., et al. 2014, *The Astrophysical Journal*, 782, 81
- Venkatakrishnan, V. 1993, in *31st Aerospace Sciences Meeting*, aIAA 93-0880
- Verbeke, C., Baratashvili, T., & Poedts, S. 2022, *A & A*, 662, A50
- Wang, H. P., Guo, J. H., Yang, L. P., et al. Submitted, *A & A*
- Wang, H. P., Xiang, C. Q., Liu, X. J., Lv, J. K., & Shen, F. 2022a, *ApJ*, 935, 46
- Wang, H. P., Zhao, J. M., Lv, J. K., & Liu, X. J. 2022b, *Chin. J. Geophys.*, 65, 2779
- Wang, Y., Feng, X. S., & Xiang, C. Q. 2019a, *Comput. Fluids*, 179, 67
- Wang, Y., Feng, X. S., Zhou, Y. F., & Gan, X. B. 2019b, *Comput. Phys. Commun.*, 238, 181
- Wu, K. L. & Shu, C. W. 2019, *Numer. Math.*, 142, 995
- Wu, S. T. & Dryer, M. 2015, *Sci. China Earth Sci.*, 58, 839
- Xia, C., Chen, P. F., Keppens, R., & van Marle, A. J. 2011, *ApJ*, 737, 27
- Yalim, M. S., Pogorelov, N., & Liu, Y. 2017, *J. Phys.: Conf. Ser.*, 837, 012015
- Yang, L. P., Feng, X. S., Xiang, C. Q., et al. 2012, *J. Geophys. Res.: Space Phys.*, 117
- Yang, L. P., Wang, H. P., Feng, X. S., et al. 2021, *ApJ*, 918, 31
- Yang, Z. C., Shen, F., Yang, Y., & Feng, X. S. 2018, *Chin. J. Space Sci.*, 38, 285
- Zhao, J., Couvidat, S., Bogart, R. S., et al. 2012, *Sol. Phys.*, 275, 375
- Zhou, Y. F. & Feng, X. S. 2017, *J. Geophys. Res.: Space Phys.*, 122, 1451
- Zhou, Y. F., Feng, X. S., Wu, S. T., et al. 2012, *J. Geophys. Res.: Space Phys.*, 117
- Zhou, Y. H., Ruan, W. Z., Xia, C., & Keppens, R. 2021, *A & A*, 648, A29

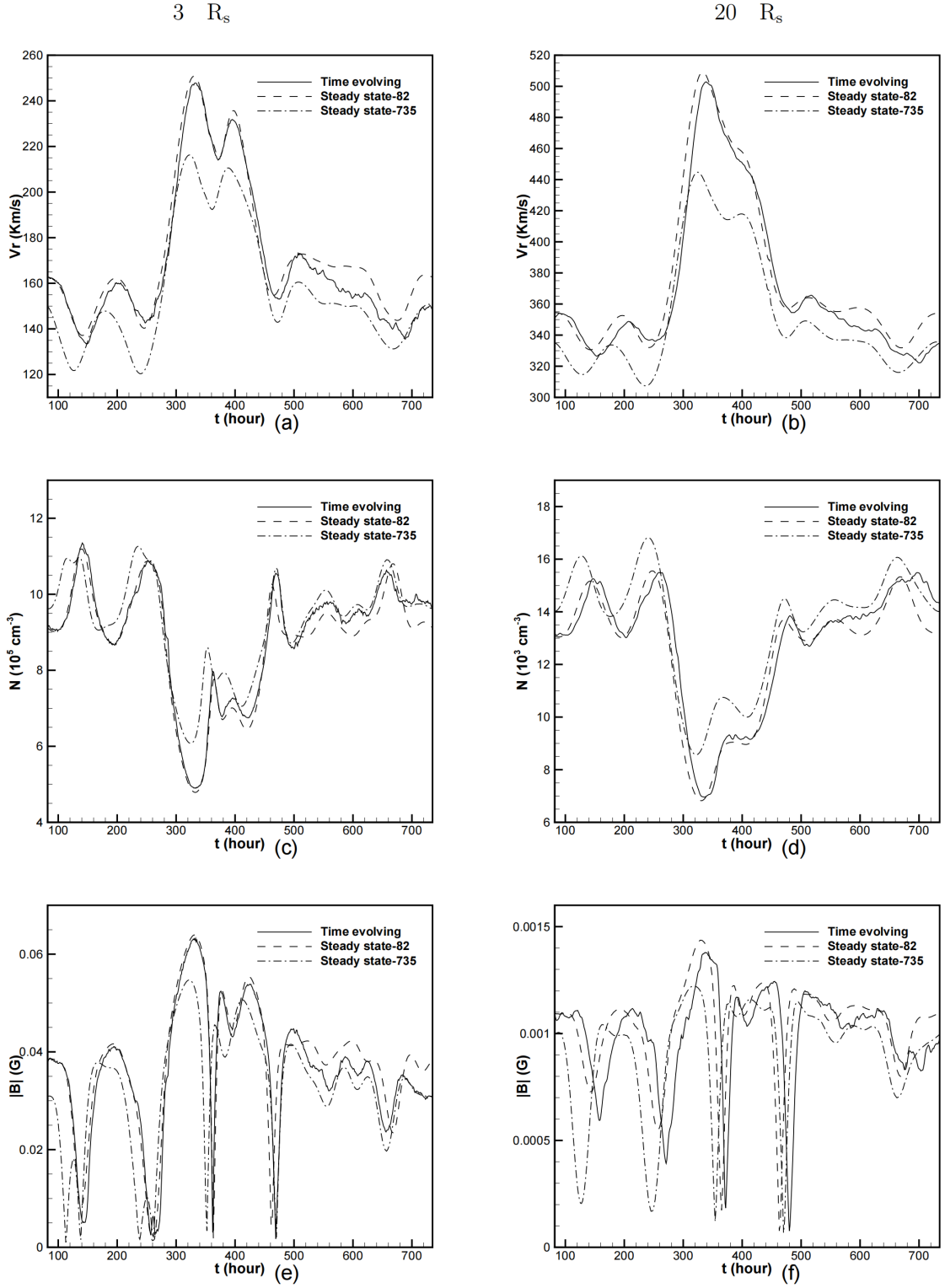


Fig. 9. Timing diagram of simulated radial velocity V_r in unit of Km S^{-1} (a, b), proton number density in units of 10^5 cm^{-3} (c) and 10^3 cm^{-3} (d), and magnetic field strength in unit of Gauss (e, f) observed by two virtual satellites located at HDLS regions. Observation points $(r, \theta, \phi) = (3 R_s, 0, 201^\circ)$ and $(r, \theta, \phi) = (20 R_s, 0, 201^\circ)$ in HCI coordinate system are selected for the time-evolving coronal simulation denoted by solid lines during the time interval between 82 and 735 hours. For the quasi-steady state coronal simulations constrained by magnetograms at the beginning (denoted by dashed lines) and end (denoted by dash-dot lines) of this time interval, the heliolongitude is mapped to a Carrington rotation period corresponding to the time series on the horizontal axis of these timing diagrams.

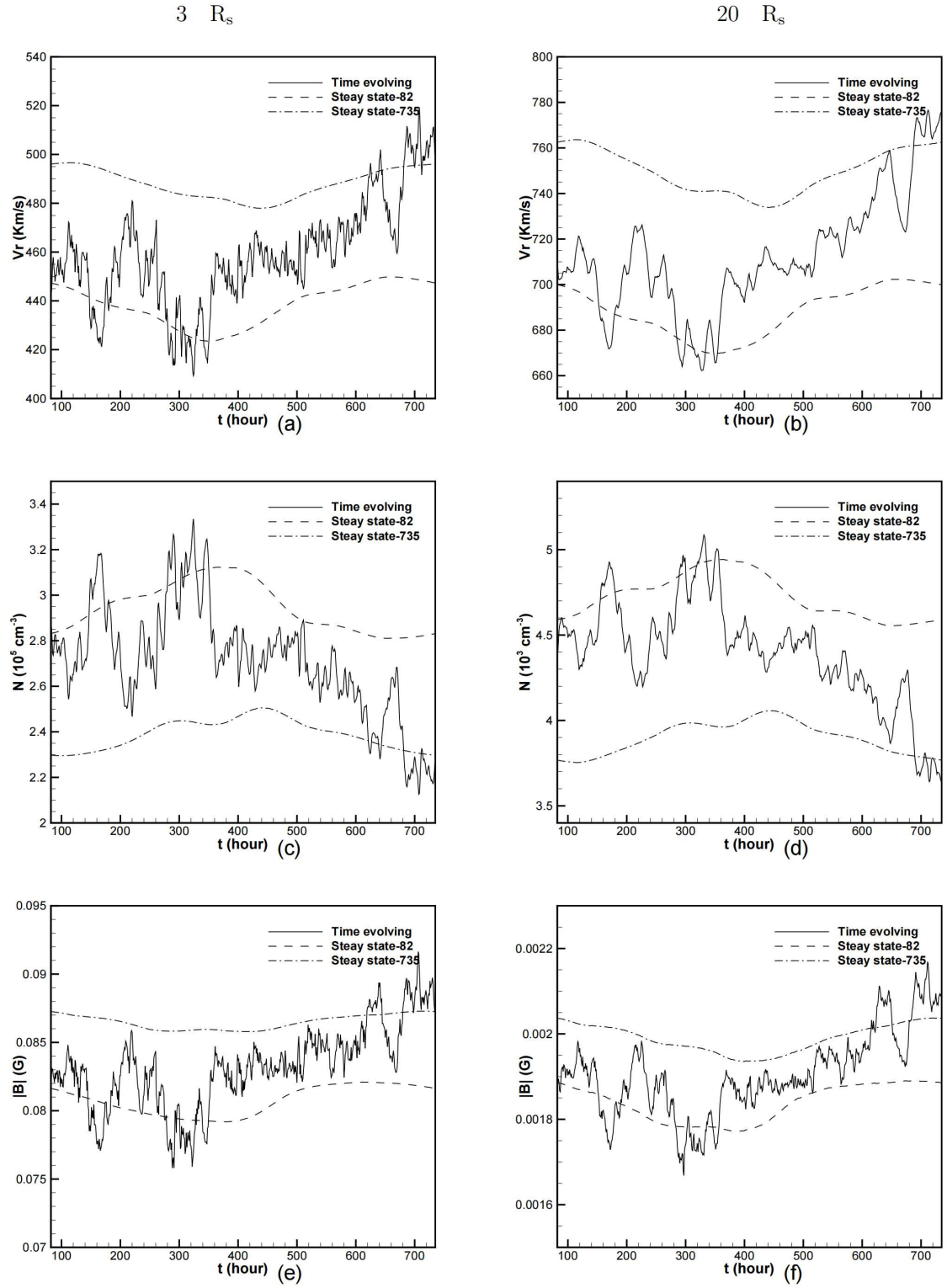


Fig. 10. The same as in Fig. 9, but with these virtual satellites located at LDHS regions, and observation points $(r, \theta, \phi) = (3 R_s, -70^\circ, 201^\circ)$ and $(r, \theta, \phi) = (20 R_s, -70^\circ, 201^\circ)$ in the HCI coordinate system selected for the time-evolving coronal simulation.

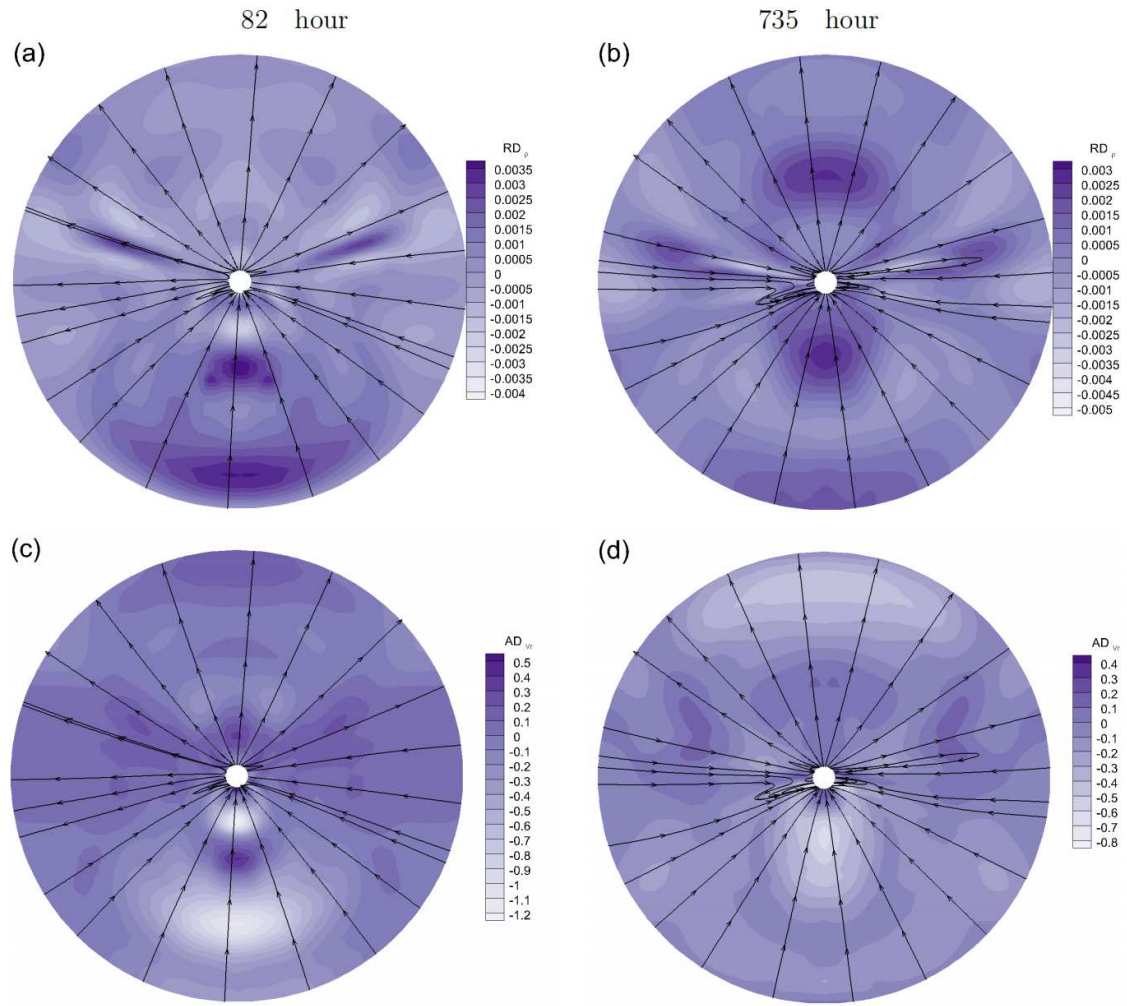


Fig. 11. Magnetic field lines from 1 to 20 R_s , overlaid on contours of the relative differences in plasma density (a, b) and absolute differences in radial velocity in units of Km S^{-1} (c, d), between the results calculated with time-step sizes of 2 and 10 minutes, on the same meridian planes as in Fig. 4.

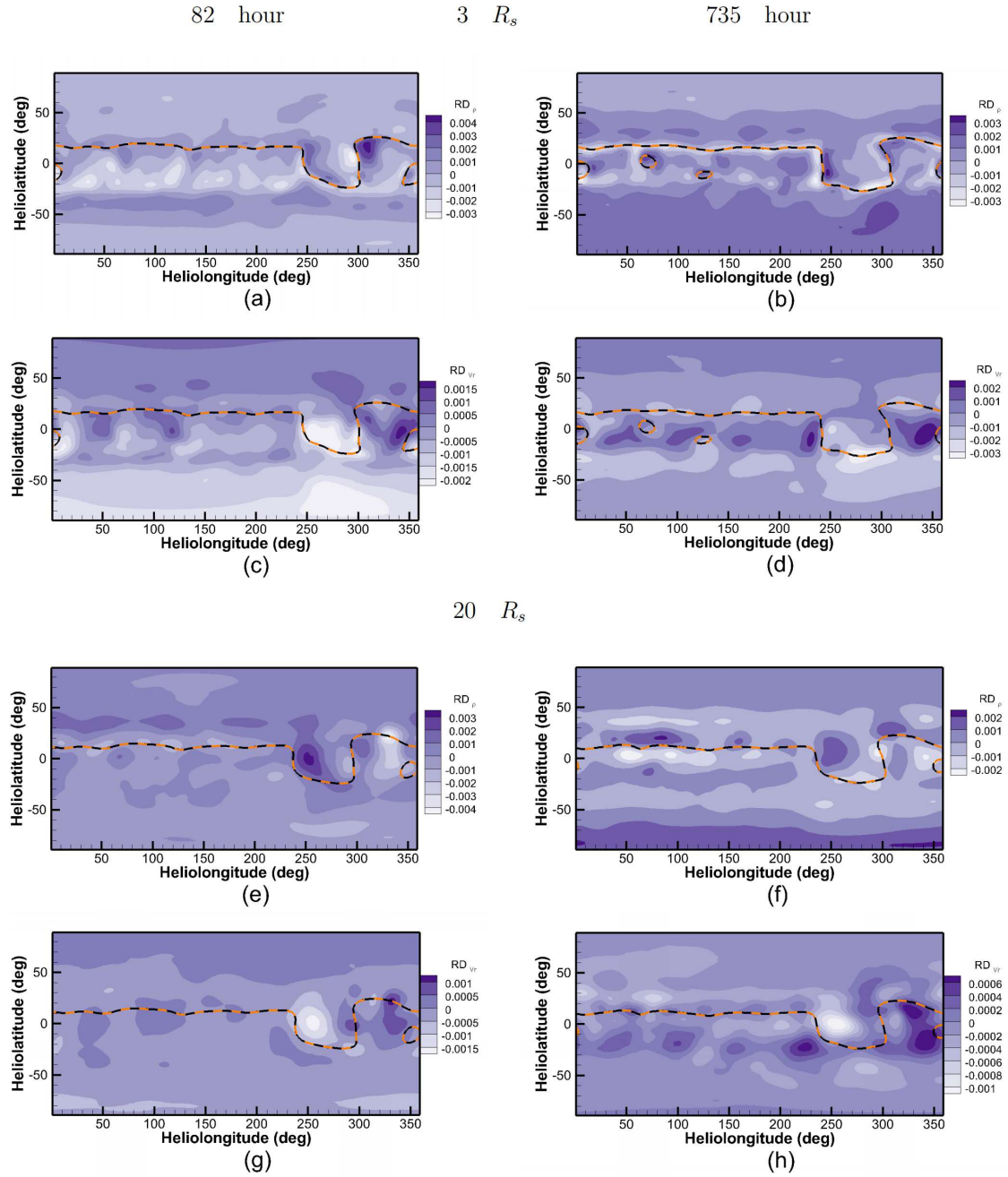


Fig. 12. Synoptic maps of the relative differences in plasma density (a, b, e, f) and radial velocity (c, d, g, h) between the results calculated with time-step sizes of 2 and 10 minutes. The black solid and orange dashed lines denote the MNLs calculated by the time-evolving coronal model with time-step sizes of 2 and 10 minutes, respectively. The locations and moments in these panels are the same as those in Fig. 6. The evolution of the relative differences in magnetic field strength at 3 and 20 R_s during the 82-nd and 735-th hours of the time-evolving coronal simulations is demonstrated in the online movies 3 and 4, respectively.

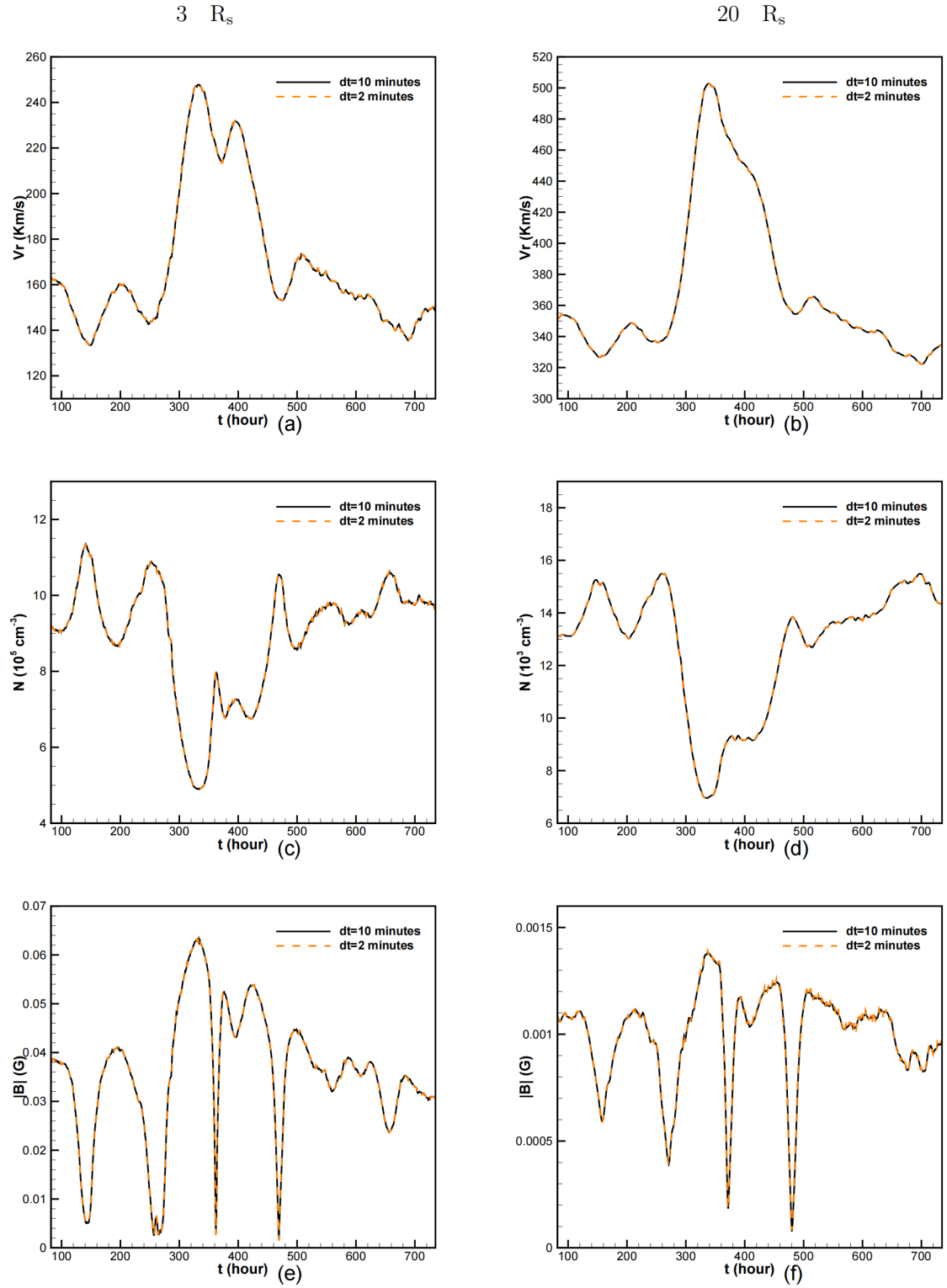


Fig. 13. Timing diagrams of simulated radial velocity V_r , in unit of Km S^{-1} (a, b), proton number density in units of 10^5 cm^{-3} (c) and 10^3 cm^{-3} (d), and magnetic field strength in unit of Gauss (e, f) observed by two virtual satellites located at HDLS regions. The black solid and orange dashed lines denote the variables calculated by the time-evolving coronal model with time-step sizes of 2 and 10 minutes, respectively. The location of these two observation points are the same as those in Fig. 9.

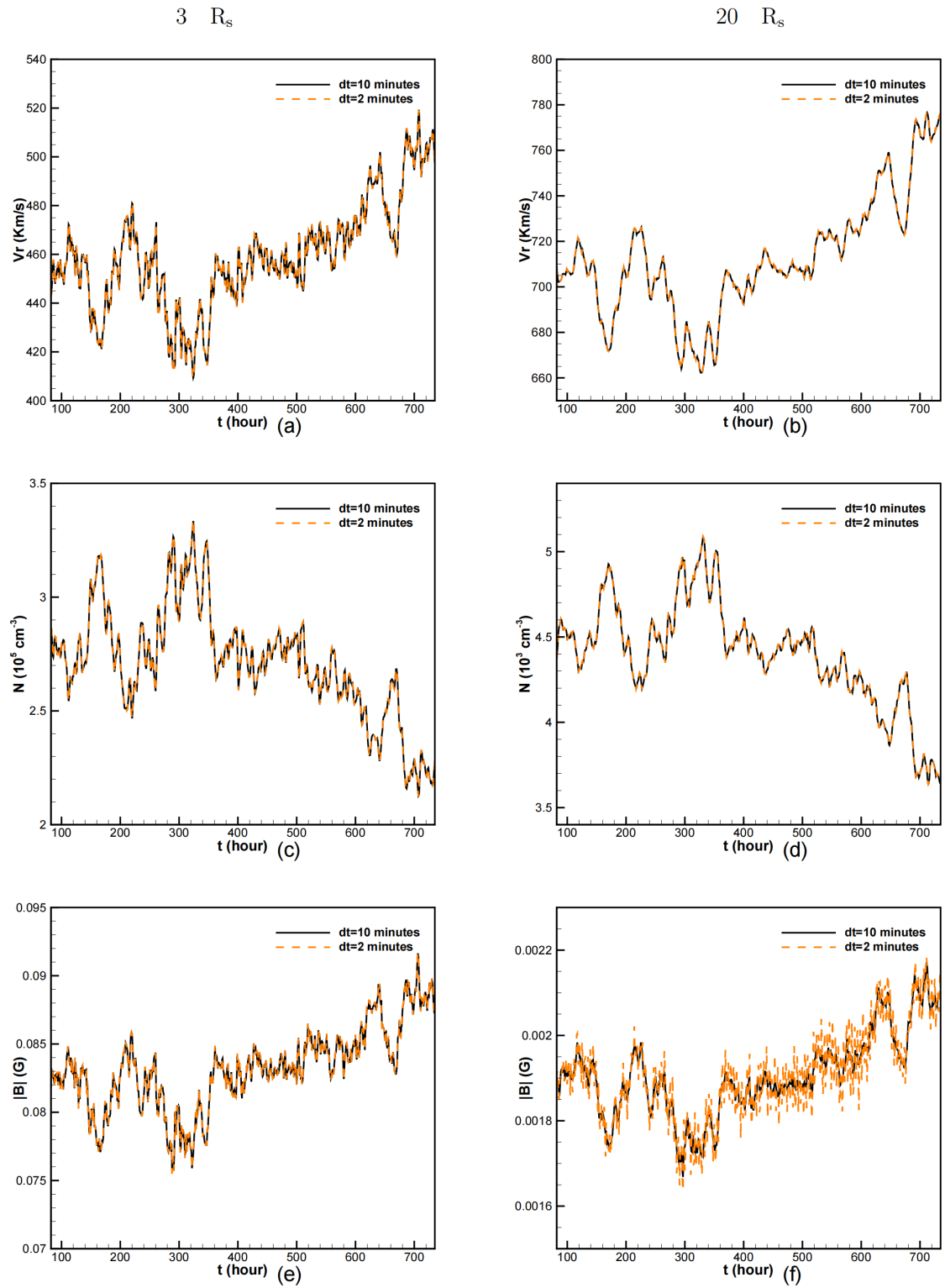


Fig. 14. The same as in Fig. 13, but with these observation points selected within the LDHS flow regions as in Fig. 10.